I. *Mariner* Mars 1971 Project

A. Project Description

The primary objective of the *Mariner* Mars 1971 Project is to place two spacecraft in orbit around Mars that will be used to perform scientific experiments directed toward achieving a better understanding of the physical characteristics of that planet. Principal among these experiments are measurements of atmospheric and surface parameters at various times and locations to determine the dynamic characteristics of the planet. Approximately 70% of the Martian surface will be observed during a minimum of 90 days of orbital operations.

During Mission A, it is planned to map the topography of a large portion of the Martian surface at a resolution significantly higher than that achievable with earth-based methods or by the *Mariner* Mars 1969 spacecraft. In addition, measurements will be made of the composition, density, pressure, and thermal properties of the planet's atmosphere. Other measurements will be directed toward an understanding of Mars' surface temperatures, composition, and thermal properties (particularly at the polar caps); its apparent lack of internal activity; its mass distribution; and its shape.

During Mission B, data will be sought on time-variable features of the Martian surface associated with the wave of darkening wherein both seasonal and secular changes occur. Also, information on atmospheric structure and gross dynamics will be obtained, as well as information directed toward an understanding of Mars' mass distribution, its shape, and its apparent lack of internal activity.

A capability will exist to redirect goals for either mission to the alternate mission if desired. The two launches are anticipated for May 1971, with arrival at the planet during the following November.

An engineering objective of the project is to demonstrate the ability of the spacecraft to perform orbital operations in an adaptive mode wherein information from one orbital pass is used to develop the operations plan for subsequent orbital passes. Studies indicate a high probability that at least one of the spacecraft will survive the sun occultation period which occurs shortly after the 90-day mission is completed. This makes it possible to conduct an Extended Mission for about a year after orbit insertion. The Extended Mission will probably consist of one or two data taking sequences per week with the capability of recording and playing back about a half-recorder of data (16 TV frames and 11 min of spectrometer data).

One of the *Mariner* Mars 1971 flight spacecraft will be new, and the other will be the spare flight spacecraft of the *Mariner* Mars 1969 Project modified to meet the requirements of the 1971 missions and to enhance mission

reliability. The proof test model spacecraft of the *Mariner* Mars 1969 Project will be modified to become the proof test model for the *Mariner* Mars 1971 Project, to be used for preliminary testing and as a simulator in support of flight operations. A major modification for the *Mariner* Mars 1971 mission will be the addition of a rocket motor required to decelerate the spacecraft and place it in orbit around Mars.

Separate scientific instrument subsystems will be required to accomplish the television, infrared radiometer, ultraviolet spectrometer, and infrared spectrometer interferometer experiments given in Table 1. The S-band occultation and celestial mechanics experiments will require no additional equipment on the spacecraft.

Management responsibilities for the overall project, the Spacecraft System, the Mission Operations System, and the Tracking and Data System have been assigned to JPL.

Lewis Research Center has been assigned management responsibility for the Launch Vehicle System. The launch vehicle will be an *Atlas/Centaur* developed by General Dynamics/Convair.

The *Mariner* Mars 1971 missions will be supported by the Air Force Eastern Test Range launch facilities at Cape Kennedy, the tracking and data acquisition facilities of the Deep Space Network, and other NASA facilities.

Table 1. *Mariner* Mars 1971 scientific experiments and principal investigators

Television	
H. Masursky	Team leader
H. Masursky	PI/U.S. Geological Survey
R. Batson	CI/U.S. Geological Survey
W. Borgeson	
M. Carr	
J. F. McCauley	
D. Milton	
R. Wildey	
D. Wilhelms	
J. Lederberg	PI/Stanford University
E. Levinthal	CI/Stanford University
J. B. Pollack	CI/Cornell University
C. Sagan	CI/Cornell University
G. de Vaucouleurs	PI/University of Texas
W. B. Thompson	PI/Bellcomm
G. A. Briggs	CI/Bellcomm
P. L. Chandeysson	CI/Bellcomm
E. N. Shipley	CI/Bellcomm
B. Smith	PI/New Mexico State University
M. E. Davies	CI/Rand Corp.
W. K. Hartmann	CI/Arizona State University
N. H. Horowitz	CI/Caltech
R. B. Leighton	CI/Caltech
C. B. Leovy	CI/University of Washington
T. B. McCord	CI/MIT
B. C. Murray	CI/Caltech
R. P. Sharp	CI/Caltech
Ultraviolet spectrometer	
C. Barth	PI/University of Colorado
C. W. Hord	CI/University of Colorado
J. B. Pearce	CI/University of Colorado

Infrared interferometer spectrometer	
R. A. Hanel	PI/Goddard Space Flight Center
B. J. Conrath	CI/Goddard Space Flight Center
W. A. Hovis	CI/Goddard Space Flight Center
V. Kunde	CI/Goddard Space Flight Center
G. V. Levin	CI/Biospherics
P. D. Lowman	CI/Goddard Space Flight Center
C. Prabhakara	CI/Goddard Space Flight Center
B. Schlachman	CI/Goddard Space Flight Center
Infrared radiometer	
G. Neugebauer	PI/Caltech
S. C. Chase	CI/Santa Barbara Research Center
H. Kieffer	CI/UCLA
E. D. Miner	CI/JPL
G. Munch	CI/Caltech
Celestial mechanics	
J. Lorell	Team leader
J. Lorell	PI/JPL
J. D. Anderson	CI/JPL
W. L. Martin	CI/JPL
W. L. Sjogren	CI/JPL
I. Shapiro	PI/MIT
M. Ash	CI/MIT
W. Smith	CI/MIT
S-band occultation	
A. Kliore	PI/JPL
D. L. Cain	CI/JPL
G. Fjeldbo	CI/JPL
B. L. Seidel	CI/JPL

PI = Principal investigator, who is the proposer for each experiment.
CI = Co-investigator, who assists the proposer on each experiment.
Team leader heads a particular group of PIs and CIs on an experiment where there is more than one PI.

B. Mission and Test Computer System,
Computation and Analysis Section

The mission and test computer (MTC) system completed the real-time system test support of the *Mariner* Mars 1971 proof-test model (PTM) spacecraft using a data system based on a single Univac 1219 computer. During this test phase the second 1219 computer was used for software development and driving video data to the mission and test video system (MTVS) to produce TV pictures. The MTC hardware system has now added a second data input subsystem, telemetry assemblers, and remote and local serial interface equipment for intercommunication with display equipment, in order to provide for the simultaneous testing of the two flight spacecraft. Dual test support, with a 1219 computer assigned to each spacecraft, began in late September 1970. By mid-October, sufficient programming development was completed to begin using the Univac 1230 MTC computer and the two Univac 1219 computers in the integrated three-computer system configuration described in SPS 37-63, Vol. I, p. 4. In this configuration the plan is for the 1230 computer to frame synchronize and decommutate all of the high-rate data streams (1–16.2 kbits/s telemetry and hardline data and 132.3 kbits/s hardline science data) and forward both the synchronized and the decommutated data to the 1219 computers for tape recording, processing, and formatting for display.

The 1230 computer decommutation programs are being developed in a sequence to provide a science instrument data-handling capability as early as possible in the flight spacecraft test program, since only a part of this data was processed during the PTM spacecraft tests. The development sequence is:

(1) Spectral science format (486 bits/frame) data decommutator.

(2) Infrared interferometer spectrometer (IRIS) science format (4725 9-bit words/frame) decommutator, for extracting IRIS interferogram data from the spectral science format as well as the recorded science format (7938 bits/frame).

(3) Ultraviolet spectrometer (UVS) science format (5400 bits/frame) decommutator, for extracting UVS instrument data from the spectral science format.

(4) UVS science format (4800 bits/frame) decommutator, for extracting UVS instrument data from the recorded science format.

(5) Video science format (972 bits/frame) decommutator.

(6) Recorded science format (7938 bits/frame) data decommutator.

(7) Orbital science format (420 bits/frame) embedded-data decommutators, for extracting the intermingled bits of the 420-bit frame from the recorded science, video science, and the spectral science data formats, simultaneously if necessary.

The 1219 computer real-time system used for PTM support provided only the recorded science decommutator capability listed above. The engineering format (140 bits frame) and orbital science format (real-time science 1) data will continue to be decommutated in real-time by the 1219 computers, as they were during PTM tests.

Magnetic tape records of all the above frame-synchronized and decommutated formats are recorded in real-time, as received from the two spacecraft. Additional records are made on this tape of the decommutated channels of engineering telemetry, orbital science data, spacecraft events and status, and central computer commands. The various intermingled records are later sorted selectively by type and re-recorded on separate types of tapes in order to save only the data required permanently. The IRIS and UVS instrument formatted records (2), (3), and (4), provide the data source for off-line processing, such as Fourier transformation of the IRIS interferogram data on the IBM 360/75 computers. The decommutated engineering and science data records provide the source for efficiently producing nonreal-time data channel tabulations and plots by the 1219 or 1218 computers without requiring decommutation, which is not available currently as a nonreal-time MTC system capability. About 400 channels of data are included in this record. Raw data records of three types are also recorded, primarily to aid in program debugging and data stream analysis. These records contain all low-rate data, all high-rate data, and the output of the data multiplexer in the attitude-control subsystem support equipment. With the exception of the recorded science format, when a data stream cannot be frame synchronized or decommutated because of erroneous PN code, wrong frame length, etc., the raw data is recorded with a suitable header identification, permitting unsynchronized data to be dumped for hand decommutation if necessary.

The 1219 computers accomplish a major portion of the general processing in the MTC system, including low-rate data stream decommutation and all tape recording functions, as well as the standard processing performed on each quantitative-measurement channel. All special processing routines required to assess spacecraft subsystem performance, extract and manipulate data, derive new data channels based on combinations of other channel data, etc., is also accomplished in the 1219s. The total processing requirements on the single 1219 computer used for PTM spacecraft test support required increasing its core memory size from 49k to 65k words by reducing the second 1219 computer to a 32k-word machine. The memory which will become available in the 65k-word 1219 computer by removal of the recorded science format (R7938) decommutator to the 1230 computer will be utilized to accommodate the program for cathode ray tube (CRT) system data display, the real-time plot processor, and additional requested special processors still under development.

The additional core memory modules required to increase the memory size of the second 1219 computer from 32k to 65k words have been obtained on loan from the USAF Space and Missile Systems Organization. This equipment was installed in late September, thus removing the limitations on dual-spacecraft test support capability and the operational inconvenience of supporting testing with different program configurations in the two 1219 computers.

Significant problems were encountered in the PTM test period in obtaining reliable frame synchronization and processing of the real-time 132.3 kbits/s high-rate science hardline data (input to the spacecraft data storage subsystem). These problems were caused mainly by deficiencies in the data interface between science support equipment and the MTC data input subsystem, which were removed by redesign, and by an intermittent failure of the interface between the data assembler and 1219 computer input channel. In addition, the programming system had to be restructured several times to eliminate saturation of the system during peak processing loads. The reliability of high-rate data processing is now satisfactory in the 1219 computer system. Checkout of the operation of decommutation programs 5, 6, and 7 in the previous list still remains to be accomplished in the 1230/1219 computer MTC system environment.

The full complement of 24 30-characters/sec printers required for displaying spacecraft subsystem and science instrument data on the two system test complexes is installed. Eight additional printers of this type (Univac DCT-500) were provided in the SFOF "mini-ops" area, a section of the future *Mariner* Mars 1971 operations area, in order to familiarize members of the spacecraft team with the format and content of the MTC-processed system test data. The 6-channel CRT display controllers (Computer Communications, Inc.) for each 1219 computer were received and are in acceptance. The leased Univac 432-drum memory system was received and is in checkout. A new motor-generator to provide 400-Hz power to the MTC system from the 60-Hz SFOF uninterrupted power system was installed to permit maintenance and repair of the second unit, following which it will become a backup power source until relocation of the prime unit at Air Force Eastern Test Range during prelaunch test. The option to purchase the Univac 1230 MTC computer was exercised at the start of FY 1971.

C. Calibration of the Scan Proof Test Model,

Spacecraft Control Section

1. Introduction

Calibration of the reference and telemetry/monitor potentiometers was performed on the scan electronics proof-test model (PTM). The calibration procedure used is new and has been developed for use on the *Mariner* Mars 1971. The reference potentiometers store the scan platform reference angles in such a way that the stored angle is proportional to the voltage on the reference potentiometer wiper. The telemetry/monitor potentiometer is mechanically coupled to the reference potentiometer and is used to monitor the position of the reference potentiometer and, hence, the stored reference angle. The stored angle may be varied in increments by stepping the reference potentiometer shaft by a drive mechanism. Calibration of the potentiometers was achieved by recording the potentiometer wiper positions as a function of a number of position increments.

2. Description of Angle Storage Subassembly

The scan subsystem contains four reference angle storage subassemblies. Each subassembly contains a stepper-motor/gear-train drive mechanism which drives a set of angle storage potentiometers. Two subassemblies with different step size are used for storing reference angles for each of the clock and cone axes as shown in Fig. 1.

In each axis one subassembly is arranged so that its stored angles can be varied in an increment of 0.25 deg (equivalent platform increment) for each command input pulse, and the other subassembly in an increment of 1 deg for each input pulse. The calibration ranges were from 90 to 305 deg in the clock axis and 90 to 170 deg in the cone axis. The fine resolution (0.25-deg increments) potentiometers were calibrated every 5 deg and the coarse resolution potentiometers (1 deg increments) every 20 deg.

3. Calibration Scheme and Results

The scan servo-control subsystem is designed to align the scan platform pointing direction with the reference angle stored in the angle storage subassembly. The pointing error generated within the subsystem is a sum of the errors contributed by the reference subassembly, the servo electronics, and the scan actuator. The error contributed by the reference subassembly is mainly caused by the uncertainty of the motor step-angle variation, gear backlash, and nonlinearity of the potentiometers. The servo electronics contributes errors due to finite gain and input offset. The actuator contributes errors due to the start voltage of the servo motor, gear stiction, and nonlinearity of the feedback potentiometer.

The calibration scheme illustrated in Fig. 2 provides information on the magnitude and characteristics of the errors contributed by the subassemblies to the subsystem pointing accuracy. Since the calibration of the potentiometers was performed without the actuator subassembly, a simulated feedback potentiometer (ratiometer 2) was inserted. The reference and telemetry/monitor potentiometers were calibrated by recording the potentiometer wiper positions in voltage ratio units as a function of a number of input pulses applied to the reference subassembly. The voltage ratio readings were obtained when the ratiometers 1 and 2 were adjusted for null on the meters M1 and M2.

The calibration of the reference subassembly revealed a typical gear backlash of about 0.02 deg (equivalent platform angle) or less. The error contributed by the motor step angle variation is non-cumulative and was

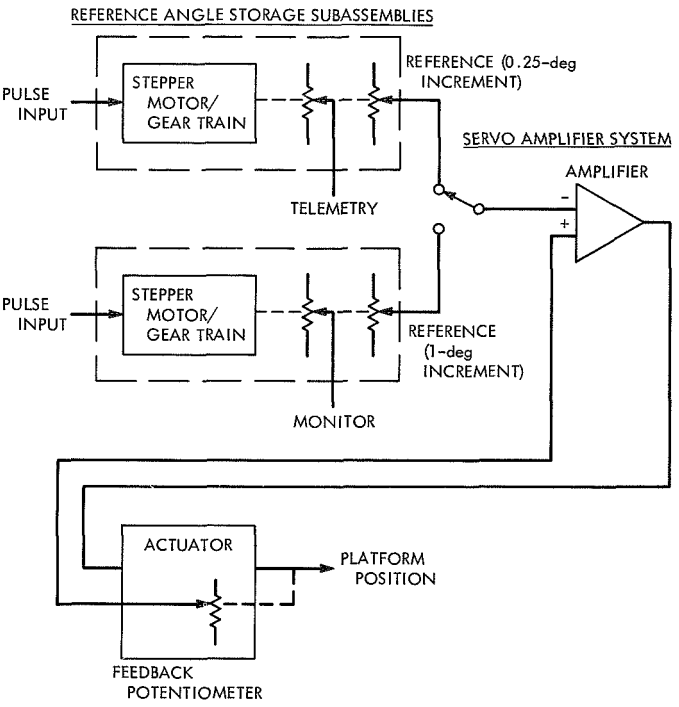

Fig. 1. Block diagram of one-axis scan subsystem showing angle storage subassemblies

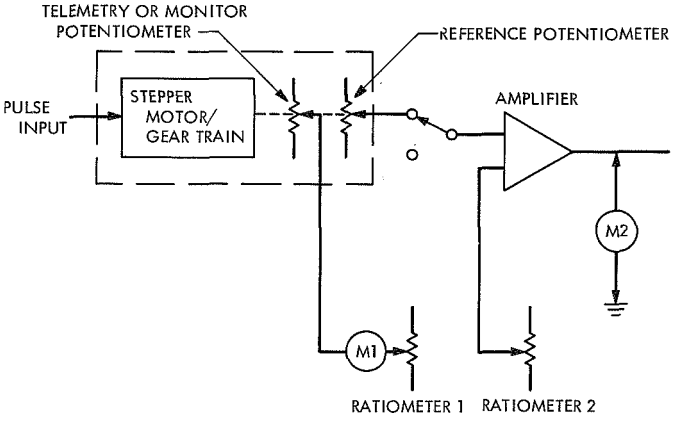

Fig. 2. Calibration scheme for one-angle store subassembly

about ±0.02 deg. The errors contributed from these sources were considered very small. The readout of the ratiometer 2 enables one to correlate the number of command input pulses to the output shaft angle of the actuator. The actuator was calibrated separately for the feedback potentiometer outputs (unloaded) as a function of the shaft angle. Since the ratiometer 2 is calibrated unloaded, its readout value corresponds to the same value on the feedback potentiometer, and hence to the corresponding actuator output shaft angle.

Using the ratiometer 2 and the meter 2, a set of measurements was taken to estimate the magnitude of the combined errors contributed by the servo electronics and the actuator. These error sources have an effect of producing an offset on the null reading of M2. During the subsystem integration test in which the servo loop was closed with the actuator, the error voltage at M2 was measured. When this value was reflected back to the ratiometer 2/M2 calibration data, the combined servo error contributed by the servo electronics, the actuator stiction and the servo-motor start voltage was determined. The magnitude of this error was 0.02 deg, which is well below the specified maximum value of 0.1 deg in an equivalent platform angle.

D. Sizing Results for Attitude-Control Gas Nozzles, *Spacecraft Control Section*

1. Introduction

One of the important activities in building an attitude-control gas system is the proper sizing of the gas nozzles to meet spacecraft control torque requirements. In order to perform this sizing, two aids are used. The first is a nozzle-sizing computer analysis program described in Ref. 1. The second is a thrust measurement stand described in detail in SPS 37-44, Vol. IV, pp. 41–42; SPS 37-50, Vol. III, pp. 112–114; and SPS 37-54, Vol. I, pp. 29–31. The procedure used was similar to the procedure developed for the *Mariner* Mars 1969 program with the following two exceptions (which necessitated additional test work):

(1) As seen from Table 1, the calculated thrust required about the roll axis is more than three times as high for the *Mariner* Mars 1971 spacecraft as for *Mariner* Mars 1969. This is due to the *Mariner* Mars 1971 requirement to counteract a potential 2 in.-lb of midcourse motor-generated swirl torque. Two inch-pounds is outside the range of the thrust stand used during the *Mariner* Mars 1969 mission, and it was necessary to extend the range and recalibrate the stand.

(2) The computer sizing program requires the discharge coefficient of the valve orifice as an input. Figure 1 is a computer-output-based curve of the thrust versus nozzle throat diameter (all other parameters held constant, as in Table 2), for two values of discharge coefficient (C_D = 0.62, 0.35). The curve indicates that the value of the discharge coefficient does not effect the thrust for levels up to 7 mlb. This is because the flow is controlled principally by the nozzle restriction (at the lower throat diameters (<0.020 in.) and not the valve orifice restriction. For the *Mariner* Mars 1969 spacecraft knowledge of the actual orifice discharge coefficient was not necessary, since the highest thrust level required was 5.43 mlb. This knowledge is necessary for *Mariner* Mars 1971, since the thrust level is 16.67 mlb. Thus, vacuum flow rate versus pressure drop tests were run to determine the correct discharge coefficients.

Table 1. Attitude-control thrust requirements

Maneuver	Principal moment of inertia, slug-ft^2	Control acceleration per half system, rad/sec^2	Moment arm, in.	Calculated thrust required for MM '71, lb	Calculated thrust required for MM '69, lb
Pitch	I_{xx} = 332	2.25 × 10^{-4}	128.5	6.97 × 10^{-3}	3.13 × 10^{-3}
Yaw	I_{yy} = 351	2.25 × 10^{-4}	128.5	7.38 × 10^{-3}	3.19 × 10^{-3}
Roll	I_{zz} = 408	[a]	120.0	16.67 × 10^{-3}	5.43 × 10^{-3}

[a]Must overcome a 2.0-in.-lb swirl torque from midcourse motor.

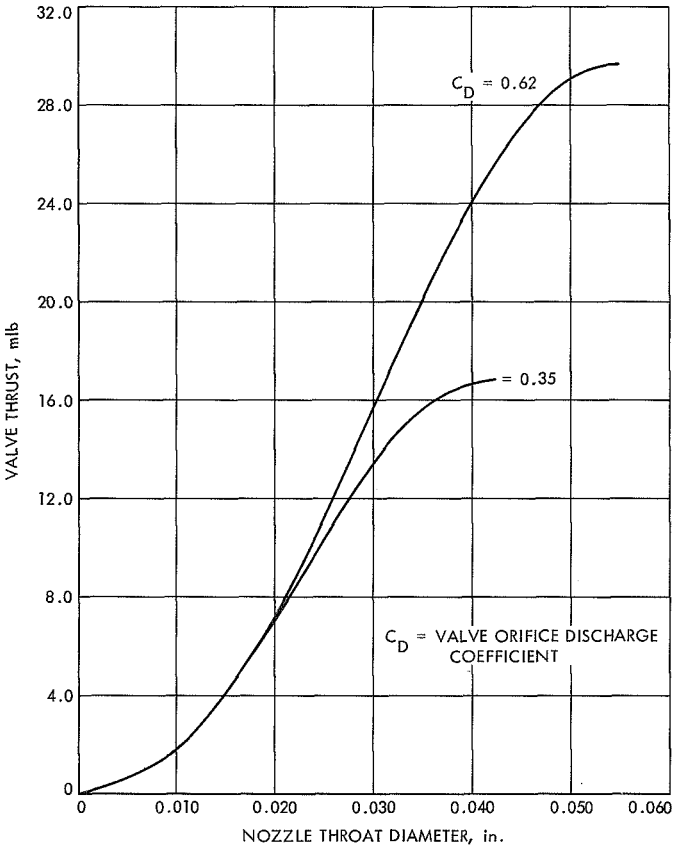

Fig. 1. Thrust versus nozzle throat diameter

2. Test Program Summary

A test program was set up to calculate the correct valve orifice discharge coefficient under vacuum conditions for various nozzle throat diameters ranging from 0.020 to 0.050 in. Flow rate and pressure drop were measured across the orifice, and the discharge coefficient was calculated. The results of this test are summarized in Fig. 2. As can be seen, the discharge coefficient varies with throat diameter. This information is then added to the computer sizing program. The results of running the program are shown in Fig. 3. The solid curve shows thrust versus throat diameter for a constant discharge coefficient of 0.62. The dashed curve shows the same results corrected for the varying discharge coefficient.

The test stand and procedure are described in detail in the SPS's in *Subsection 1.* Basically, the test setup is a vertical cantilever beam (also used as the gas feed line) pinned at the top. The valve and manifold are mounted at the bottom and at right angles to the beam. Displacement of the beam caused by the thrusting is measured by a differential transformer pickoff and recorded on a

Table 2. Initial conditions for nozzle-sizing computer program

Parameter	Value
Valve discharge coefficient	0.35, 0.62
Valve ball travel, in.	0.0068
Ambient temperature, °C	25
Valve ball diameter, in.	0.188
Valve seat diameter, in.	0.132
Nozzle geometric area ratio	50:1
Nozzle exit geometry half-angle, deg.	25
Ratio of specific heats (nitrogen)	1.4
Nitrogen gas constant, ft-lbf/lbm-°R	55.16
Ambient pressure, psi	0
Valve inlet pressure, psi	15.0
Nozzle throat diameter, in.	0.010 to 0.050 (variable)

strip chart recorder. Damping was supplied with a mercury bath and paddle. A hanging steel ball is used for calibration. The tests were run in a vacuum. Three changes were made to this test stand for the *Mariner* Mars 1971 program. The first was minor modifications to the calibration fixtures to facilitate the larger calibration range required. The second was the replacement of the pressure gauge used to measure valve inlet pressure with a pressure transducer for faster response. The third was to increase the amount of damping by changing from mercury to Dow Corning DC200 (25,000 cS). The resulting extended calibration curve is shown in Fig. 4. This curve is slightly nonlinear at the high end. Five test

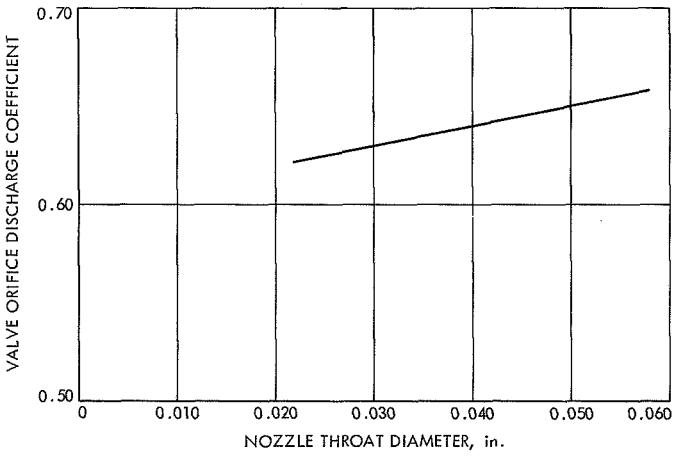

Fig. 2. Valve orifice discharge coefficient versus throat diameter

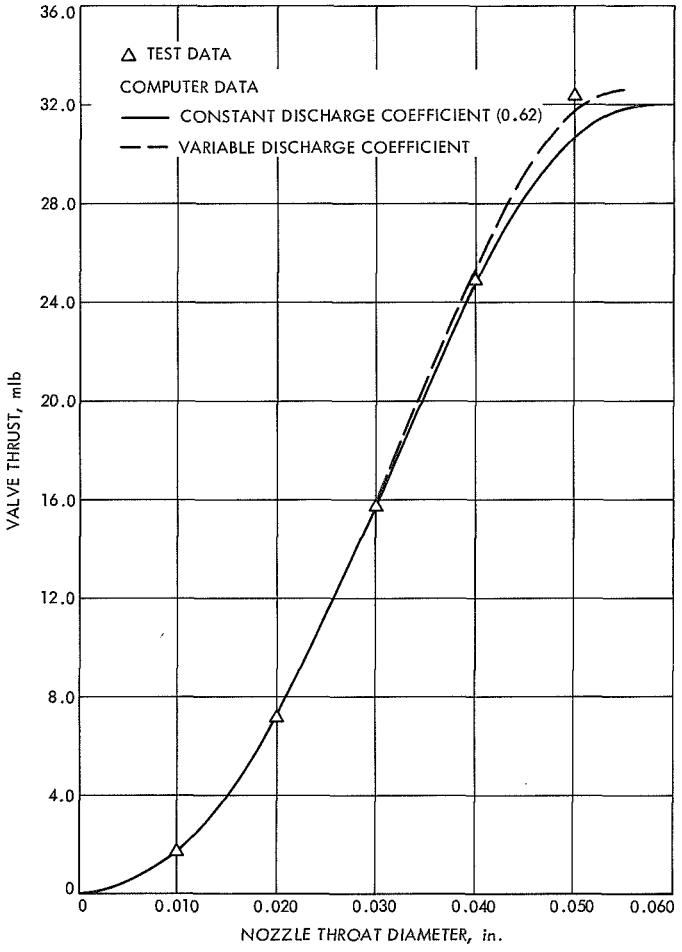

Fig. 3. Valve thrust versus nozzle throat diameter

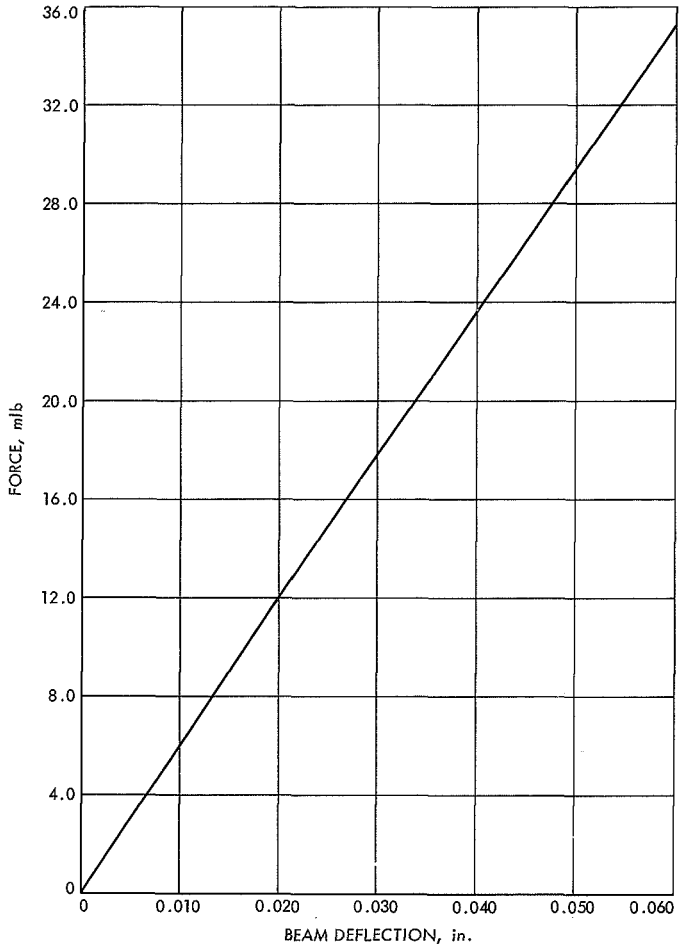

Fig. 4. Thrust stand calibration curve

nozzles were run, and the results are plotted as triangles on Fig. 3.

3. Conclusions

The following conclusions can be drawn from the above activity:

(1) The test range of the thrust stand has been extended from 10 to 32 mlb.

(2) The resulting agreement between test data and the computer program output is within 1% up to throat diameters of 0.40 in.

(3) All information required is available to completely specify the nozzles to be fabricated for the *Mariner* Mars 1971 spacecraft.

Reference

1. Ferrera, J. D., and McKown, P. M., "A Method for Calculating Steady-State Thrust and Flow-Rate Levels for *Mariner IV* Type Attitude Control Nitrogen Gas Jets," Technical Report 32-1353, Jet Propulsion Laboratory, Pasadena, Calif., Dec. 1, 1968.

E. Modeling of a Peripheral Belt Drive Magnetic Tape Transporter, *Spacecraft Data Systems Section*

1. Introduction

Since its rather recent inception, the peripheral belt drive mechanism for moving magnetic tape has continued to gain popularity, particularly in the field of satellite and deep space onboard recorder/reproducer subsystems. The peripheral belt concept offers several unique advantages over other more conventional approaches, including relatively low power consumption, light weight, improved packaging efficiency, and increased reliability. A further advantage is the adaptability of this type of drive to a wide range of tape widths, lengths, and tape elastic characteristics. Perhaps its most significant advantage is the way in which tape tension is developed by the mechanism. The peripheral belt drive develops tape tension as a function of the reel geometry, belts and tape elasticity, tape length, head drag, and the relationship of belt and tape membrane thicknesses. The tape tension is independent of power source, tape speed, and servo design. The tension does not depend on a stable reel torque bias as is the case with drives utilizing Negator-type spring motors or torquer reel motors. As such, the stability of the tension profile is dependent only on the characteristics of elasticity, friction, and geometry.

Because of the many advantages of the peripheral belt drive over some other types, it was selected for use in the *Mariner* Mars 1971 tape transporter. Although the drive concept had proved its feasibility prior to the time of selection for the *Mariner* Mars 1971 mission, it had not been adequately mathematically modeled to the point of a thorough understanding of the mechanism. Several attempts had been made to model the drive, with unacceptable results. Modeling the mechanism required a thorough understanding of elasticity and insight into the limits of a repetitive process.

Early in the developmental stages of the *Mariner* Mars 1971 program, one of the more common problems of low-speed recording developed. Tape stick-slip (random incremental tape velocity) was observed in the transporter. Stick-slip was clearly unacceptable. The reliable performance of the data storage subsystem depended on the ability of the transporter to move tape by the heads at a uniform velocity. It thus became clearly necessary to understand the mechanisms of the tape drive as it relates to stick-slip and that the problem be confronted on several fronts. The thorough understanding of the tape tension, tension variation, and mechanism for developing tape tension was considered imperative, since it became clear that stick-slip occurred at the tape-to-head interface. Toward this end, a rigorous analytical model of the transport drive was developed by the Engineering Mechanics Division at JPL. The quasistatic analysis was used to develop an expression for take-up tension as a function of: (1) pay-out tape tension, (2) deck reel and idler geometry, (3) static force and moment equilibrium, (4) belt and tape elasticity, (5) magnetic head drag, (6) tape length, and (7) the relationships between belt thickness and tape thickness.

2. Analytical Model

Figure 1 illustrates the general configuration of the *Mariner* Mars 1971 transporter tape deck. A tensioned seamless polyester drive belt (peripheral belt) is routed around the perimeter of the assembly simultaneously driving both the pay-out tape reel and the take-up tape reel. The belt transmits its motion into the tape packs via the friction interface between the belt and tape. As such, the stability of tape motion depends on establishing a nonslipping belt to drive/driven elements interface. The belt is driven by a capstan referred to as the "fast" capstan. The connotation comes from a condition where one of the two capstans is required to rotate with a greater peripheral velocity than the other, thus the distinction of fast capstan and slow capstan is applied. The slow capstan is caused to rotate with a lesser peripheral velocity than the fast capstan so that it appears as a load element to the motion of the peripheral belt. The two capstans are coupled by an elastic drive belt. The ratio of capstan velocities is referred to as the capstan differential and is nominally calculated from geometry assuming an infinitely stiff coupling belt. The load presented to the belt by the slow capstan requires that a tension change occur across the capstan. It can be shown by taking moments about the slow capstan that the belt tension approaching the slow capstan will be less than the tension leaving the capstan by an amount equal to the term $2\alpha\Delta T$, where α is the ratio of capstan input pulley diameter to capstan diameter, and ΔT is the tension difference developed in the capstan coupling belt. The increased tension in the belt leaving the capstan results in a reduced cross-sectional area of belt.

In order that continuity of mass flow in the belt be preserved, the velocity of the belt leaving the capstan must be greater than the velocity of the belt approaching the capstan. Thus, a tension and velocity differential is established across the slow capstan such that the velocity of the belt approaching the take-up reel tends to

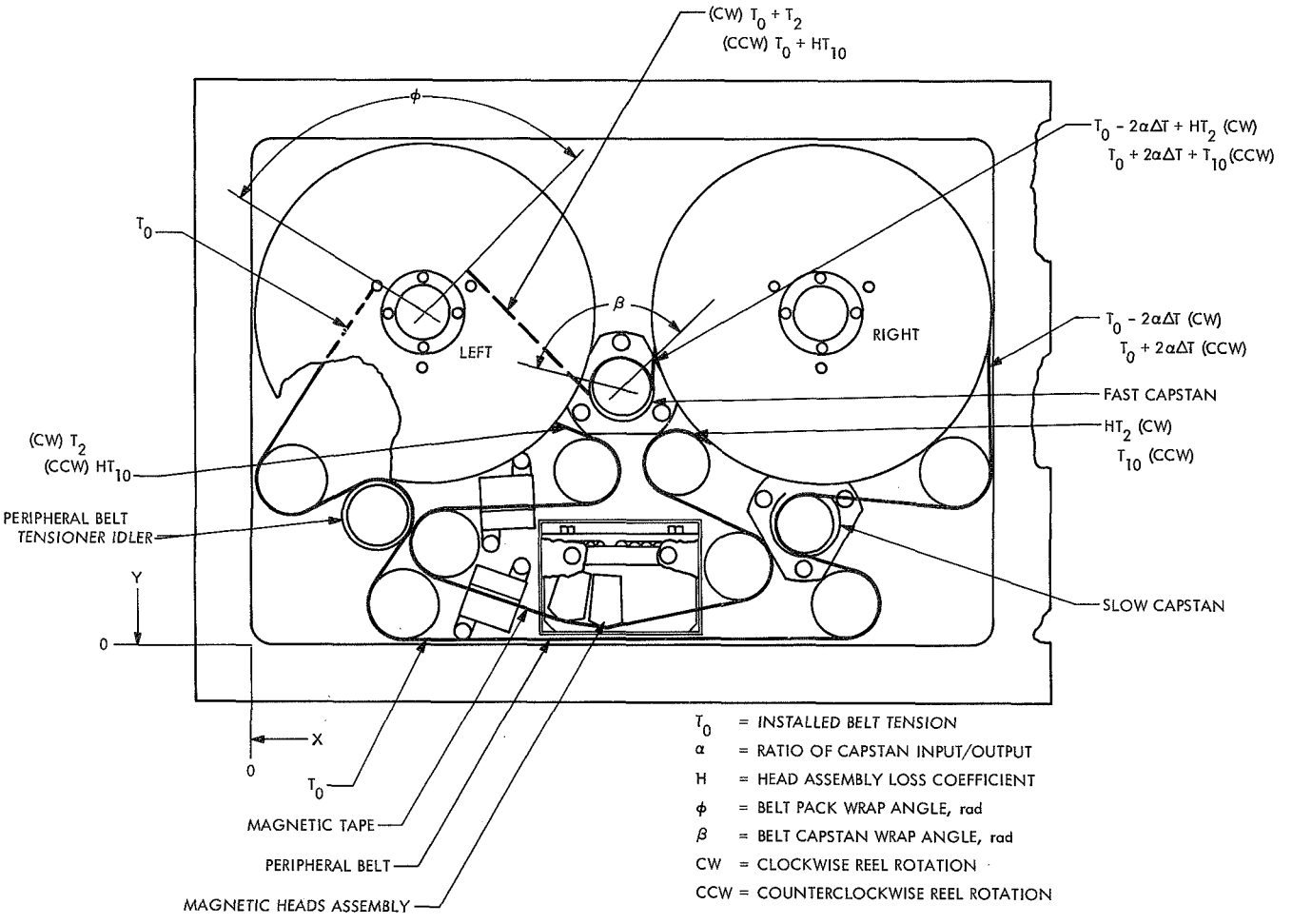

Fig. 1. Transport deck layout (top view)

be greater than the velocity of the belt leaving the pay-out reel. Note that the belt will neither pile up on itself nor fail in tension, since the mass flow is maintained as constant at any point in the path. The expression for tape tension is slightly different, depending on which reel is the take-up reel (tape direction). The difference results from geometrical asymmetry of the tape deck. It is assumed that no slip occurs on the leading edge of the capstans or tape packs with the belt, although some creep of the belt is required if a belt tension change is to occur. An "equilibrium" tape tension exists such that the take-up tension tends toward the pay-out tension (it must be remembered that the present pay-out tension is the previous take-up tension). The deviation from this equilibrium tension at the take-up reel is a constant ($0 < k < 1$) times the deviation at the pay-out reel. The tension does not approach the equilibrium tension as a limit because the tape motion is bidirectional, alternating between the two reels. If the tape motion were unidirectional, the take-up tension would equal the equilibrium tension in the limit. However, there exists an equilibrium tension loop, formed by the two tape direction tension curves, such that if the tension on the pay-out reel is on one branch of the loop, the pay-out reel will transfer to the take-up reel with a tension equal to the other branch of the loop. The general case of an equilibrium loop is shown in Fig. 2a. The loop has been referred to as a "bow tie" profile.

The analysis can be repeated assuming slippage occurs at the slow capstan. A different equilibrium loop will result yielding a lower level of tension characterized by excessive tension spikes just prior to the tape direction reversal. The analysis is carried through by assuming a variable differential and reducing the value of the differential to the point at which slip is impending. The time rate of change in tension is found to be sufficiently small to warrant omission except at the transition from

take-up to pay-out, which occurs during a direction reversal. At this time, a tension peak is formed causing the tension to approach the hypothetical equilibrium limit associated with the direction of prior motion.

As a result of the analysis, several changes were implemented in the transporter to: (1) reduce the average tape tension at the heads and reduce the range of tape tension and (2) remove certain instabilities (i.e., capstan slippage) that existed in the tape drive. Figure 2a illustrates a typical tension profile measured prior to the changes. Figure 2b illustrates the improved profile resulting from the analysis. The analytical model has been verified in accuracy by numerous tests of different configurations and represents a very powerful tool for optimization of a particular peripheral belt drive. The most significant parameter in establishing a uniform tape tension over the tape length was found to be the radial distance separating the elastic center of the peripheral belt from the elastic center of the magnetic tape. Reduction of the peripheral belt thickness and modulus of elasticity are the most important parameters to reduce mean take-up tension as well as making it more uniform. The complexity of the expression for tape tension is such that one must be very careful in generalizing the effect of one parameter variation on the tape tension.

The proper design of a peripheral belt drive must take into consideration not only tape tension, but also (1) capstan slippage, (2) belt/tape pack slippage, (3) head drag,

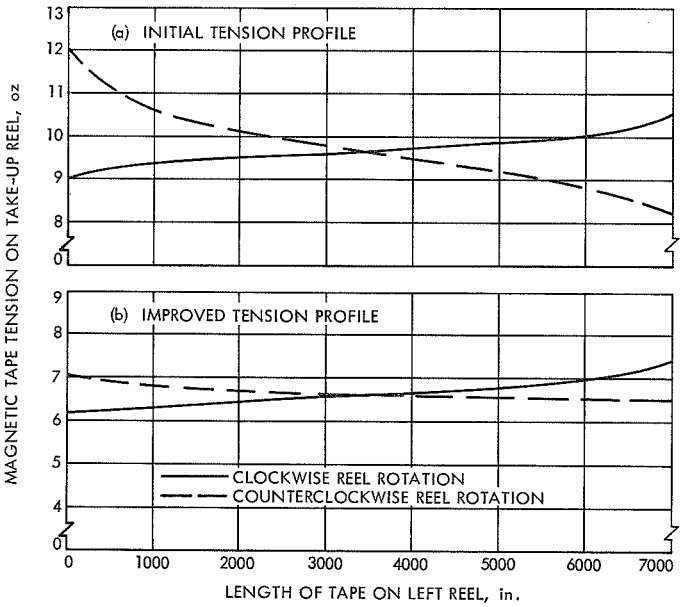

Fig. 2. Magnetic tape tension profiles

(4) membrane stress and fatigue levels, and (5) drive system torque transmissibility. In the final analysis, stability of tape motion and tension can be assured only if proper attention is given to the total design of the drive mechanism. Considering the unique geometric and elastic relationships of the *Mariner* Mars 1971 transporter, some specific statements can be made about ramifications of some single parameter variations. Some of the more interesting are listed in Table 1.

Table 1. Parameter variations

Variation	Effect
Capstan coupling belt stiffness	Changes tape tension. Little effect on tension range
Peripheral belt width	Changes tape tension. Little effect on tension range
Magnetic tape modulus	Changes tension range. No effect on average tape tension
Magnetic tape thickness	Changes both average tension and tension range
Capstan differential	Changes average tension. No effect on range
Peripheral belt thickness	Changes average tension and range.
Head Loss	Changes average tension. Little effect on range

Because of its dependency on elasticity, tape tension is sensitive to temperature changes to the same degree that the membrane elastic modulus is sensitive to temperature changes. In designing a peripheral belt transporter to operate under wide temperature limits, one must consider the possible changes in elastic properties of belts and tape. A properly analyzed drive would express the elastic constants as functions of temperature, as indeed they are. This understanding could lead to a temperature-compensating design which would set the tape tension as a constant and yield the required temperature–elasticity relationships between the various elastic elements. A further approach would be to fabricate the capstans each of materials different in temperature expansion characteristics so that the tendency toward elastic change would be negated by a change in capstan differential.

3. Conclusions

As a result of the analytical modeling, the mechanism inducing tape tension is more clearly understood. Many variables are involved in the development of tape tension. The complexity of the expressions does not allow

generalization of parameter variation ramifications, nor can an analysis performed for a particular set of deck geometry be directly applied to a different set of geometry. The complexity of the mechanism requires that the breadboarding be first done analytically and that parameter variations be explored in the same manner. Any commitment to develop a peripheral belt drive for a particular requirement should include the commitment to fully model the transport analytically prior to accepting the design.

F. Propulsion Subsystem, *Liquid Propulsion Section*

1. Introduction

The *Mariner* Mars 1971 spacecraft incorporates an on-board modularized propulsion subsystem to furnish impulse to the spacecraft for trans-Mars trajectory correction, orbit insertion, and orbit trims. The propulsion subsystem operates on liquid propellants: nitrogen tetroxide (N_2O_4) and monomethylhydrazine (MMH). The subsystem is a regulated-pressure constant-thrust system employing: (1) gaseous nitrogen pressurant stored at 3650 psia within two 15-in.-diam titanium vessels, (2) Teflon-bladdered 30-in.-titanium propellant tanks, capable of storing 635 lb of N_2O_4 and 410 lb of MMH, (3) two pressurant check and relief valve assemblies, (4) explosively actuated isolation valves in both the pressurant and liquid circuits, and (5) a 300-lbf-thrust conduction-cooled rocket engine.

2. Effects of Propellant Saturation With Gaseous Nitrogen on Hydraulic Resistance

Rocket engine tests using nitrogen-saturated propellants were conducted early in the engine prequalification test program. These tests verified previous test indications that saturated propellants produce an increase in the oxidizer flow circuit hydraulic resistance resulting in decreased oxidizer flowrate and engine mixture ratio. The magnitude of this mixture ratio decrease was from 5 to 8% for full saturation at propellant tank pressures of 250 psig. The allowable mixture ratio uncertainty for the *Mariner* Mars 1971 propulsion subsystem is $\pm 3\%$. Therefore, it was obvious that propellant saturation would have to be a major consideration in the characterization of the *Mariner* Mars 1971 engine operation.

Two basic approaches were considered to obtain the test data necessary to characterize engine performance with saturated propellants:

(1) Expand the engine prequalification and qualification test programs to obtain the basic performance characterization with additional testing at the subsystem level for verification.

(2) Initiate cold-flow testing of a breadboard system using simulated or flight-like components with verification tests at the engine or subsystem level.

The cold flow test approach was chosen primarily on the basis that cold-flow testing could be conducted with minimum interference to current component test programs. Greater flexibility in terms of configuration and test operation, and reduced cost per test were also decided advantages.

3. Discussion

The simulated oxidizer flow circuit consisted of six thin flat-plate orifices as shown in Fig. 1. The orifices were sized to simulate the pressure losses of the principal subsystem components: propellant standpipe, squib valve package, filter, engine calibration orifice, propellant valve, and injector.

Pressure transducers were used to determine the pressure drop across each orifice. Turbine-type volumetric flowmeters, one upstream and one downstream of the orifices, were used to determine the flowrate.

Propellant saturation was accomplished by bubbling gaseous nitrogen through the propellant for approximately one-half hour while maintaining the proper backpressure. The propellant then remained undisturbed for one-half hour before a propellant sample was drawn from the tank.

Flow tests using first nonsaturated and then saturated oxidizer were conducted with no measurable change in hydraulic resistance in any of the orifices. The increased speed of the downstream flowmeter during the saturated tests indicated the presence of evolved gas. Orifices 3 and 5 were removed and replaced by a 30-μm flight-type filter and a flight-type propellant valve. The flow tests were then repeated with no change in hydraulic resistance.

A simulated oxidizer injector plate was designed and fabricated to replace orifice 6. The simulated injector contained the same number of orifices, the same nominal orifice size, and the same orifice L/D as the *Mariner* Mars 1971 engine injector. The flow tests were repeated, and an increase in the injector resistance was noted with saturated propellants. Additional testing was conducted with the oxidizer saturated at various pressure levels. The resulting resistance increase with gas saturation is presented in Fig. 2. Several data points from the engine margin limit test program are also shown for comparison. The resistance increase is plotted against the volume of gas out of solution upstream of the injector. Good agreement is shown between the cold-flow data and the engine test data.

The volume of gas out of solution was calculated, based on the injector inlet pressure and Henry's constant for solubility.

$$V_{out} = V_{tank} - K(P_{inj} - P_v)$$

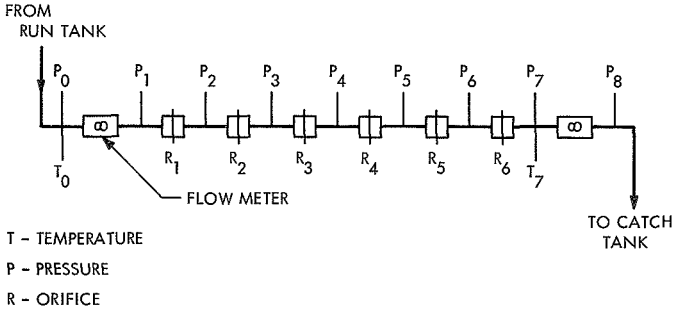

Fig. 1. Flow bench schematic

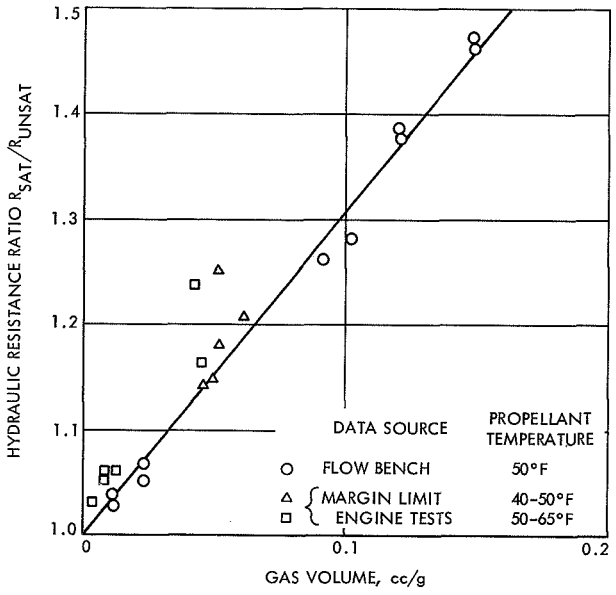

Fig. 2. Injector resistance for nitrogen-saturated oxidizer

where

V_{out} = volume of gas out of solution, standard cc/g

V_{tank} = volume of gas in solution at the propellant tank, standard cc/g

K = Henry's solubility constant — 0.01 scc N_2/psi-g oxidizer

P_{inj} = injector inlet pressure, psia

P_v = vapor pressure of oxidizer

This method and the data plotted in Fig. 2 were used to predict propellant consumptions for the engineering test model and type-approval model test programs. Propellant consumptions were predicted on the oxidizer side for both saturated and unsaturated conditions to within 1%.

Tests were also conducted with saturated fuel (monomethylhydrazine) using an orifice plate simulating the engine fuel injector orifices in a flow bench configuration. These tests revealed the resistance increase for full saturation to be about 1%. This agreed with engine test results, but some system tests have indicated a possible increase in fuel resistance of about 2%. This result is currently being investigated.

4. Conclusions

The following conclusions can be drawn, based on the results of nitrogen-saturated propellant tests conducted in support of the *Mariner* Mars 1971 propulsion subsystem development program:

(1) The volume of nitrogen which remains in solution is directly related to the partial pressure of the nitrogen for both oxidizer (N_2O_4) and fuel (MMH).

(2) The primary increase in resistance due to evolution of dissolved gas occurs in the relatively long orifices ($L/D = 10$) of the rocket engine injector.

(3) The increase in resistance across the injector is proportional to the volume of gas out of solution upstream of the injector orifices as indicated in Fig. 2 for the oxidizer.

(4) The increase in injector resistance in the fuel flow circuit with saturated propellant was about 1% for full (250 psig) saturation.

G. Effect of Solvent on the Biaxial Properties of Liquid Propellant Expulsion Teflon Bladder Bags, *Polymer Research Section*

1. Introduction

Standard laminate Teflon bladder bags employed as liquid propellant expulsion devices for the *Mariner* Mars 1971 spacecraft have been failing due to the formation of tears and cracks near an aluminum seal ring which forms the mouth of the bag. These failures were occurring during flight-acceptance tests in which various solvents were used as referee fuels. From a consideration of the conditions imposed on the bags during the tests, it was recognized that the neck region of the bags are biaxially stressed while at the same time being bathed by the test solvent. A previous report (SPS 37-65, Vol. I, pp. 40–42) has demonstrated that standard laminate is extremely sensitive to solvent, a property which results in a marked reduction in the materials uniaxial stress–strain properties. This report gives the results of a study on the effects of solvent on the biaxial properties of standard laminate materials. Also included are test results obtained on a new candidate material designated "codispersion laminate," as well as a study of the effect of solvents on FEP 120, FEP 9511, and TFE 30, the Teflon components which are used in the construction of the laminate materials.

The effects of these solvents on the biaxial properties of standard and codispersion laminate were as follows:

(1) Standard laminate is sensitive to solvent and fails from solvent-stress cracking at strains less than 6% when biaxially stressed. This characteristic is undoubtedly the prime cause of failure of standard laminate bladder bags when exposed to solvent during flight-acceptance tests, where failure occurred from the formation of cracks and tears in the highly biaxially stressed neck regions of the bladder bags.

(2) Codispersion laminate, on the other hand, offers a significant improvement in resistance to solvent-stress cracking. The poorest case is for Freon-TF exposure, wherein biaxial failure occurs at 28% strain. However, presoaking in Freon-TF prior to biaxial testing results in a significant increase in strain at failure from 28 to 128%.

(3) A study of the solvent sensitivity of FEP 120, FEP 9511, and TFE 30, revealed that only FEP 120 is significantly solvent sensitive. This material, not used in codispersion laminate, is a major component of standard laminate and must, therefore, be labeled as the dominant contributor to the solvent sensitivity of standard laminate. This is further substantiated by the experimental observation that surface crazing which precedes the failure of the standard laminate in solvent occurs in FEP 120.

2. Experimental

a. Biaxial test. The biaxial test consisted of straining a test sample whose width is very large compared to the test length. In this way, as the material is strained by a uniaxial extension along the test length, the large width will prevent the material from necking, thus creating a transverse biaxial stress. In uniaxial testing, where the

test width is small compared to the test length, the necking which occurs as yield stress is approached causes the test width to be diminished due to the Poisson effect. In the current test, the material is constrained against transverse necking; and, as a result, a biaxial stress field is imposed on the sample.

The biaxial test specimen is shown in Fig. 1a. The dotted parallel lines are employed during test to allow visual verification that no transverse contraction is occurring, while the two solid lines are grid lines employed for strain determination. They are separated by 0.5 in. and positioned symmetrically around the center point. Crosshead speed on the Instron is 0.2 in./min which allows time to observe the specimen as well as to monitor the grid line separation for strain measurements. One half inch of the top and bottom of the specimen are held by the biaxial Instron grips. Details of the test set-up and immersion bath are shown in Fig. 1b.

The solvents employed were heptane, isopropyl alcohol, and Freon-TF. The latter two solvents were selected because they are employed as the referee fluids in the flight-acceptance testing of the bladder bags, while heptane was included because it has a known effect on Teflon materials.

b. Bladder construction details. Details of construction of the bladder bags are shown in Fig. 2. Standard laminate is a two-ply construction consisting of one ply of FEP 120 and another ply of TFE 30. Codispersion laminate is a three-ply construction consisting of an inner ply of FEP 9511, while the two outer plys are formed from a codispersion of 80% TFE 30 and 20% FEP 9511.

3. Results

a. Biaxial test on standard laminate. A summary of the biaxial stress–strain properties for the standard laminate is shown in Fig. 3. The solid line is the stress–strain curve obtained for three control specimens which were tested in air, showing the positions at which each of the specimens failed. The strain at break ranged from 40 to 108%, and inspection of the failed specimens revealed a correlation between the strain at break and the extent of delamination of the two plys along the fracture line. The sample failing at low strain underwent very extensive delamination, whereas the sample failing at high strain showed no evidence of delamination. This is reasonable, for it is known (Ref. 1) that FEP 120 fails biaxially near 30% strain, and TFE 30 fails near 270% of strain. Hence, if delamination occurs, there is no reinforcement of the weaker FEP 120 by the stronger TFE 30 and a low strain failure will occur.

For the solvent study, samples were tested after initial exposure to solvent and after a two week presoak. Though no effect of aging of the material in solvents was observed, the overall effect of solvent was significant. The solid symbols on the solid line in Fig. 3 locate the positions at which the standard laminate materials failed biaxially. The effect is dramatic, for it was found that standard laminate fails at strain levels less than 6% as a result of solvent exposure. Since these strain levels are easily achieved by the bladder bag when filled with solvent and subjected to flight-acceptance test, the solvent-stress cracking of standard laminate emerges as the prime mechanism of bladder bag failure. This can be seen further by comparing the formation of cracks and tears in the biaxial test samples, as shown in Fig. 4, with the same sequence of events occurring to the bladder bags, shown in Fig. 5.

Figures 4a and 5a show the initial formation of surface crazing, while Figs. 4b and 5b show the resultant formation of a crack. For the biaxial test specimen, this was considered failure and corresponds to the dark symbols on the stress–strain curve in Fig. 3. Figure 4c is a close-up detail of the crack separation in the biaxial sample. Figures 4d, 5c, and 5d detail the subsequent tearing of the material after the crack separation has occurred.

b. Biaxial test in codispersion laminate. Codispersion laminate offers significant improvement in the resistance to solvent–stress cracking. This can be seen in the biaxial stress–strain results for isopropyl alcohol and heptane exposure shown in Fig. 6, and for Freon-TF exposure shown in Fig. 7. Although the displacement of these curves from the control indicates some solvent effect, the strain at break is still high for biaxially applied stresses. Further, the fractures were clean, with no delamination, and with no crazes or cracks occurring on the surface of the materials prior to break.

The only solvent effect of any significance occurred for sample exposure to Freon-TF, where the strain at break was at a surprisingly low 28% (curve I in Fig. 7).

Since this low strain was observed on specimens tested immediately after exposure to Freon-TF, samples were presoaked for periods up to 2 wk and then tested with the result (curve II in Fig. 8a) that the strain at

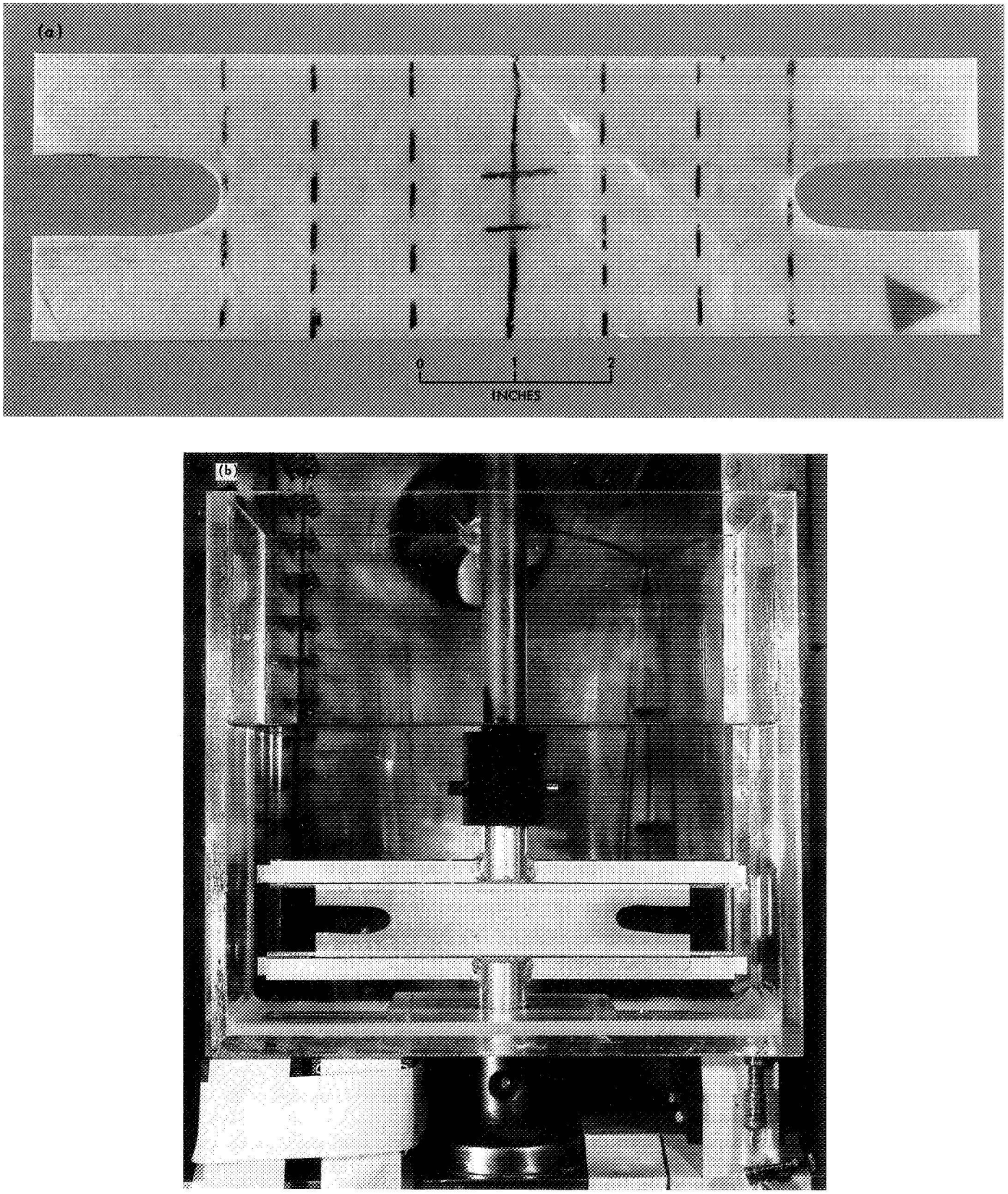

Fig. 1. Biaxial test specimen and test apparatus with immersion bath

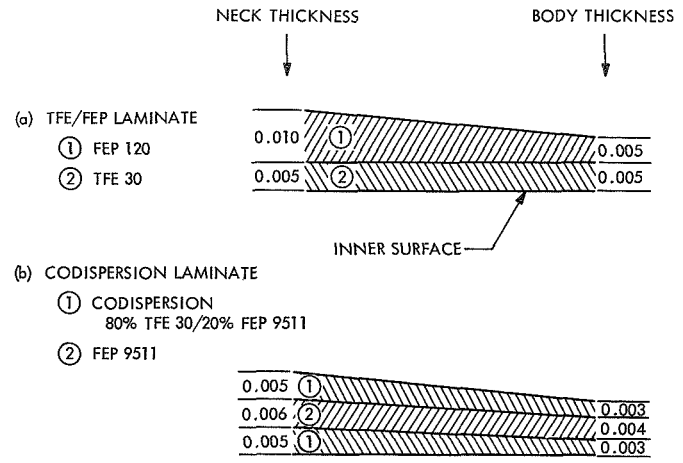

Fig. 2. Bladder construction details

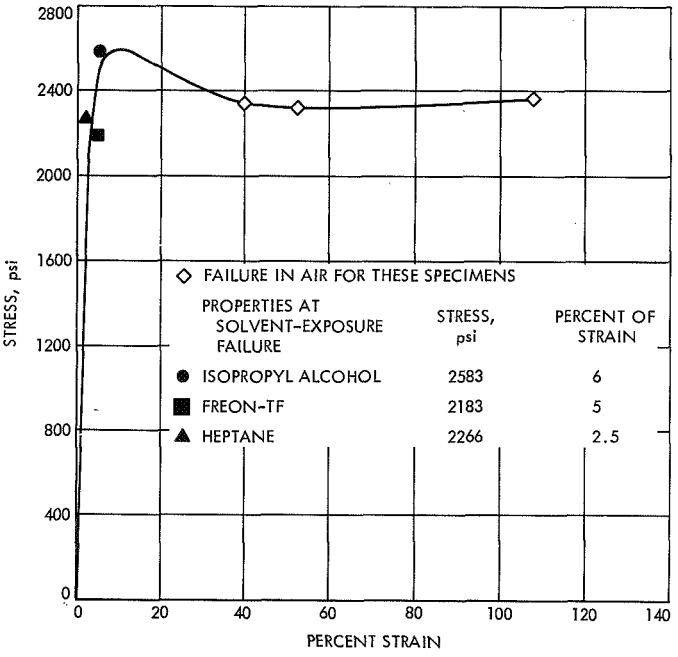

Fig. 3. Biaxial stress–strain properties for standard laminate

break increased to 128%. A speculation on the origin of this effect will be discussed under the section on fracture mechanics. There was no effect from pre-soaking codispersion laminate in heptane and isopropyl alcohol.

c. Solvent studies of bladder bag components. The effect of solvent on the bladder bag components FEP 120, FEP 9511, and TFE 30 was assessed by measuring the uniaxial stress–strain properties of these materials while they were completely immersed in solvent. The

Table 1. Effect of solvent[a] on bladder bag components FEP 120, FEP 9511, and TFE 30

Component	Percent of Crystallinity	Yield stress, psi	Ultimate stress, psi	Ultimate strain, %
FEP 120	29			
Tested in air		2188	3380	435
Freon-TF		1998	2031	124
Heptane		2077	1854	148
Isopropyl Alcohol		2118	3253	399
FEP 9511	22			
Tested in air		2034	3569	362
Freon-TF		1882	4459	408
Heptane		1965	3566	334
Isopropyl Alcohol		1998	3536	323
TFE 30	45			
Low crystallinity				
Tested in air		1421	4968	590
Freon-TF		1276	4983	639
Heptane		1329	4926	568
Isopropyl Alcohol		1471	5479	548
TFE 30	73			
Middle crystallinity				
Tested in Air		1641	3732	695
Freon-TF		1777	2597	570
Heptane		1835	3306	517
Isopropyl Alcohol		1786	4045	580
TFE 30	83			
High crystallinity				
Tested in air		1937	3686	681
Freon-TF		1870	3120	564
Heptane		1934	3539	515
Isopropyl Alcohol		1973	3641	447

[a]Assessed by measuring the uniaxial stress–strain properties while immersed in solvent. In Fig. 9, a typical stress–strain curve is shown for these materials when tested in air. Solvent exposure does not alter the basic shape of the curve, but can affect the magnitude of the stress and strain at break (ultimate properties), and the yield stress. Solvent attack is identified by a decrease in ultimate strain, while plasticization is identified by a decrease in yield stress.

results (Table 1) reveal that FEP 120 is extremely solvent-sensitive, while FEP 9511 and TFE 30 are virtually resistant to any solvent attack. Thus, the solvent sensitivity of standard laminate appears to be related to the FEP 120, a conclusion further supported by the experimental observation that the surface crazing

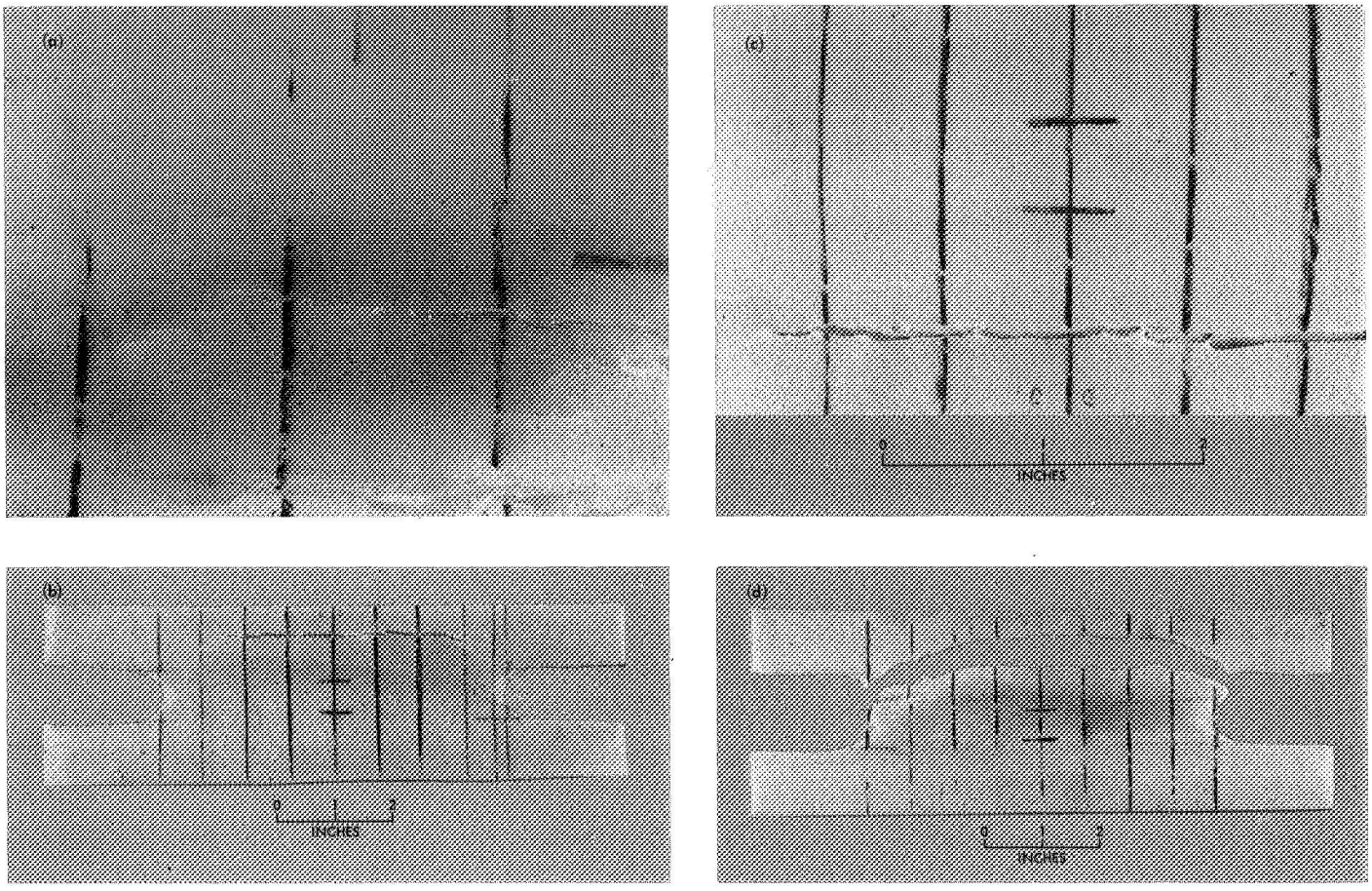

Fig. 4. Failure of standard laminate in solvent: (a) surface crazing in FEP 120 layer for biaxial strains from 1 to 5%, (b) cracks forming from crazes adjacent to Instron grips, (c) close-up detail of crack, (d) resultant tear from crack

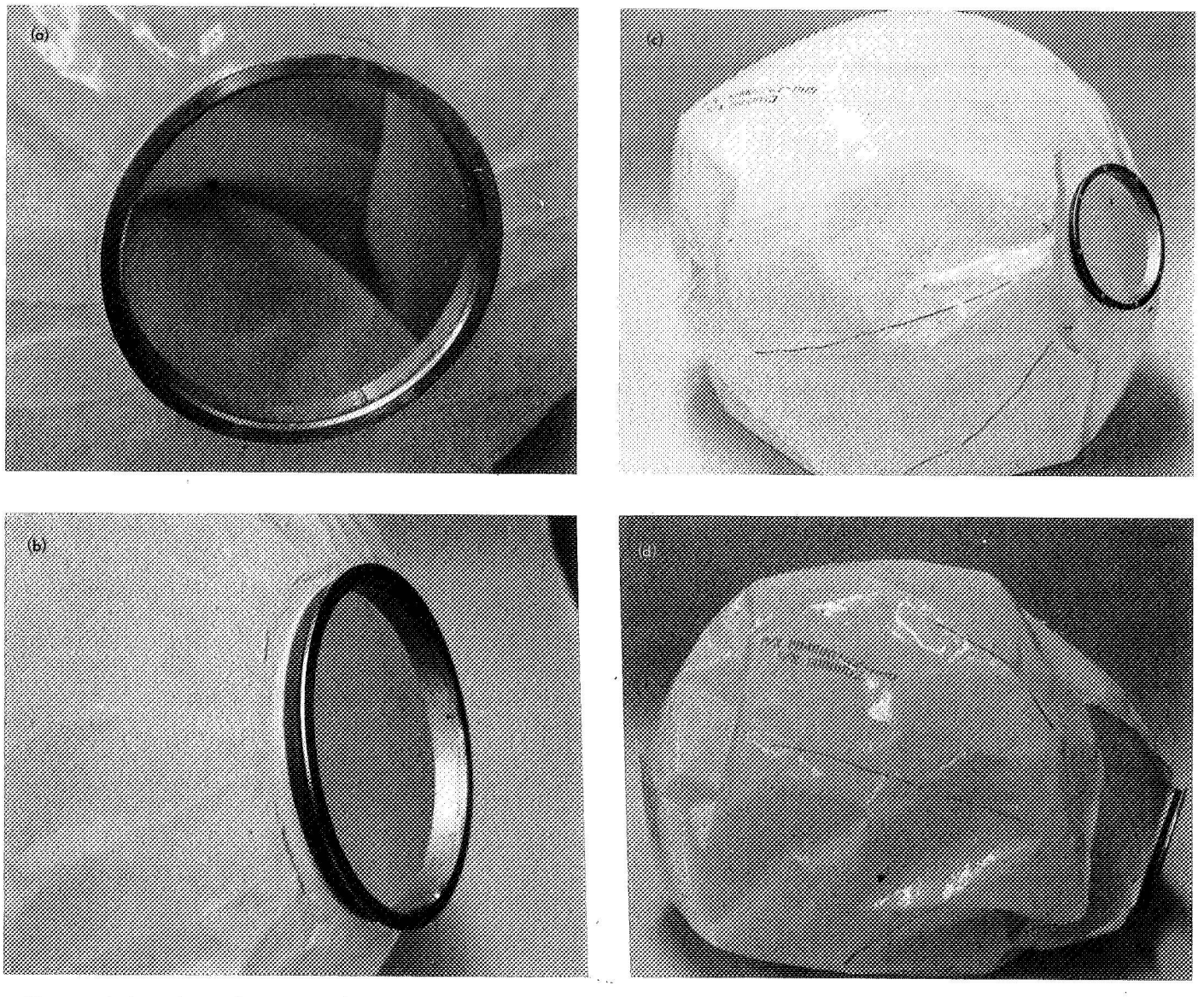

Fig. 5. Failure in neck region of standard laminate bladder bag: (a) crazing from solvent exposure, (b) cracks, (c) tearing resulting from cracks, (d) advanced tearing and total failure

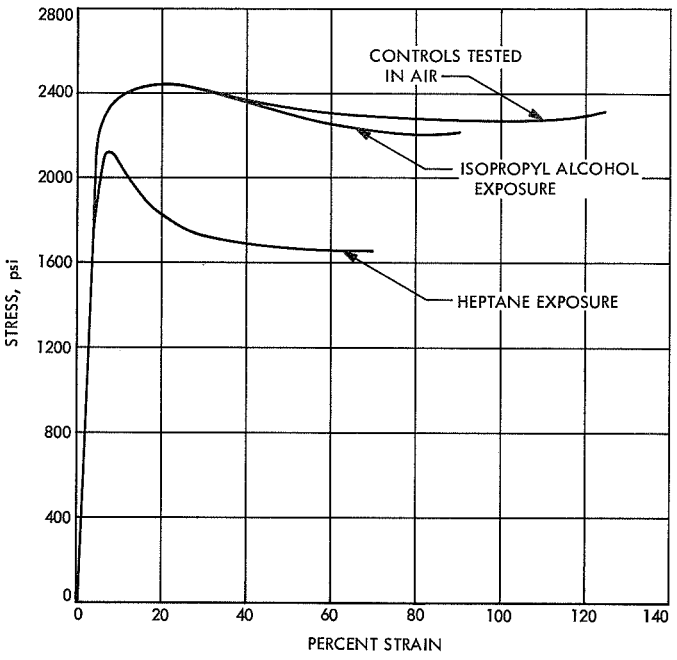

Fig. 6. Biaxial stress–strain properties for codispersion laminate

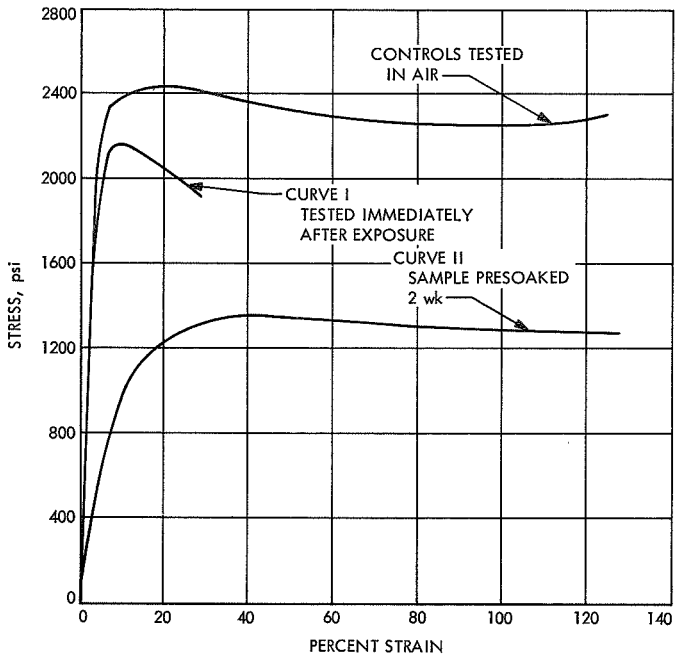

Fig. 7. Biaxial stress–strain properties for codispersion laminate exposed to Freon-TF

of the standard laminate (Fig. 4a) always occurs on the FEP 120 side.

d. Fracture mechanics. The significance of the failure of the biaxial specimens to the failure of standard laminate bladder bags and the low strain failure of Freon-TF exposed codispersion laminate is discussed here.

The fracture line for both standard and codispersion laminate air-tested samples occurred in the central portion of the specimen (Fig. 8a and b), as it also did for the codispersion specimens tested in heptane and isopropyl alcohol (Fig. 8c). However, the fracture line for the codispersion laminate initially exposed to Freon-TF and for all the solvent-exposed standard laminate specimens occurred (Fig. 4b) along a straight line which was parallel to and within 0.25 in. of the Instron grip. For the standard laminate, the fracture separation occurred in a craze which had previously developed adjacent to the grip, while the Freon-TF exposed codispersion laminate specimen developed no crazes or cracks prior to failure and broke cleanly at 28% strain. These observations were repeatedly confirmed.

Thus it must be concluded that for standard laminate, failure in the presence of solvent begins with the development of surface crazes in the FEP 120 layer at very low strains ($<< 6\%$), and those crazes which are immediately adjacent to where the material is mechanically constrained (i.e., Instron grips) develop into the cracks which characterize the failure of standard laminate. These observations from the biaxial testing explain why the crack separations occur in the neck, because it is here where the material, as in the Instron grips, is both biaxially stressed and mechanically constrained by being bonded to the aluminum seal ring. Further, presoaking of standard laminate prior to test does not affect either the low strain at failure or the location of the fracture line.

Presoaking codispersion laminate in Freon-TF, however, results in both a change in the level of strain at failure and the location of the fracture line, which moves up into the central portion of the test specimen. And, there is no crazing in the material to account for the low strain failure. Therefore, the low strain failure of the Freon-TF exposed codispersion laminate must arise from a different mechanism.

It is known that Freon-TF will swell codispersion laminate. Hence, speculatively, initial exposure to Freon-TF could have resulted in swelling of the free central portion of the specimen while that portion in the Instron grips is mechanically prevented from swelling.

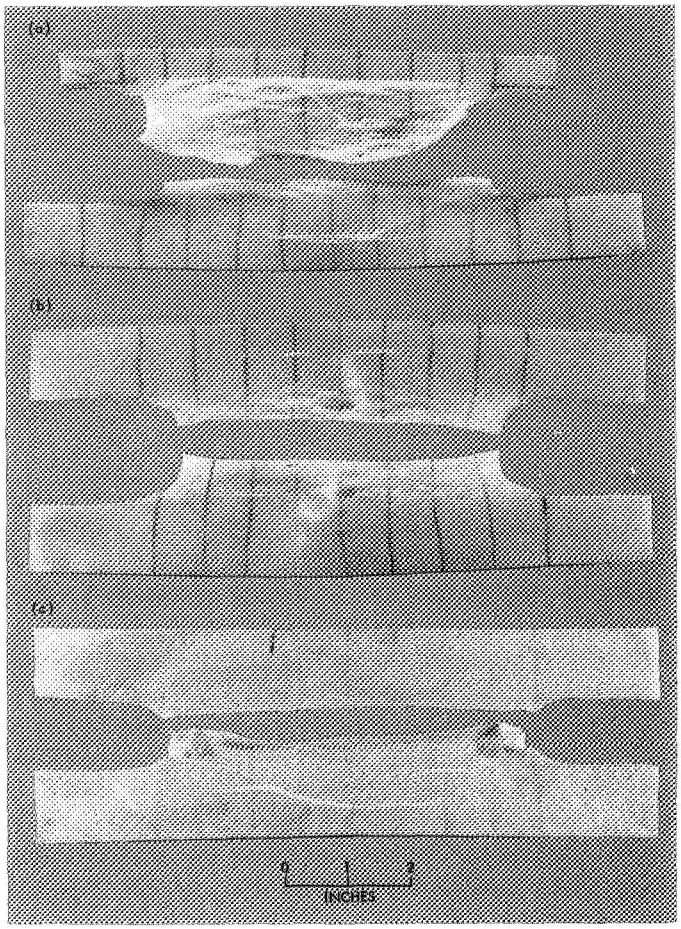

Fig. 8. Fracture lines for: (a) air-tested standard laminate, (b) air-tested codispersion laminate, (d) solvent-tested codispersion laminate

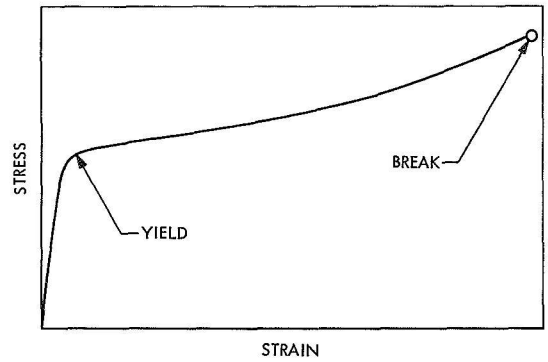

Fig. 9. Stress-strain curve typical of Teflon bladder bag materials

Thus, this may have established a differential stress across the material at the boundary of the grip, a stress sufficient to lead to premature failure near the grip. Presoaking the material prior to test allows the whole specimen to swell, and this acts to prevent the conditions leading to the premature failure.

If this hypothesis has any merit, some attention may have to be given to the flight-acceptance testing of codispersion laminate bladder bags when Freon-TF is employed as a referee fuel.

Reference

1. Krusos, J. N., Higgins, R. G., and W. H. Dukes, *Design Criteria and Quality Control Studies for Teflon Expulsion Bladders,* Report 8460-933012, Bell Aerosystems Company, March 1967.

H. Spacecraft Mass Property Determination,

Advanced Projects Development Section

1. Mass Property Requirements

The spacecraft weight and approximate center-of-mass are required for launch vehicle performance calculations. The weight must also be known to calculate spacecraft ΔV capability. Both center-of-mass and inertias are needed for autopilot stability and performance analyses. Inertias are also required for attitude-control gas consumption estimates. All mass properties are needed for spacecraft/launch vehicle separation analysis.

2. Mass Properties Assignments

All mass properties control, as well as publishing and transmitting mass properties information to interested persons, was handled by the System Design Section in the Project Engineering Division. Examples of control are the establishing of weight allocations, establishing center-of-mass envelopes, and resolving violations (or anticipated violations) of these. The Engineering Mechanics Division determines the mass properties, and maintains the following information:

(1) Current mass properties for components from the subsystems.

(2) A component properties list sufficiently detailed to provide a reasonable input to the mass properties computer program.

(3) A mass properties computer output of current estimates of spacecraft mass properties.

(4) Measurements of spacecraft mass properties.

(5) Periodic reports of spacecraft mass properties to the System Design Section.

3. Analytical Activities

The bookkeeping system selected was an indented list corresponding to the spacecraft drawing tree. This list is referred to as the weight list by drawing tree, or simply the master list.

Each line contains four entries: part number, description, reference designation, and current weight. The reference designation is the designator given the formal equipment and weight list (M71-3-230). The reference designation is included on the master list so that a list by subsystem can be generated. The last entry is the current weight. The value of the current weight is a representative or typical value for the flight part. In contrast to the system for the *Mariner* Mars 1969 spacecraft, no attempt is made to keep track of the actual weights of various serially numbered parts.

The weight list by drawing tree requires two types of information: format information and weights. From this weight list, two other lists were generated. One was the mass properties computer program input; the other was the subsystem or weight list by subsystem, which is generated by sorting on the reference designation entry in the master list. The subsystem list is generated for use by the Systems Design Section for mass property control.

A reference designation of 2000 is used for items that are not delivered to the spacecraft assembly facility as part of a subsystem. This is mainly system level installation fasteners (e.g., screws, cable clamps, etc.).

The mass properties computer program requires as input the weight, center-of-mass location, and local moments and products of inertia for each item on the spacecraft. It computes the weight, center-of-mass location, and inertias for the composite spacecraft. The inputs to the program are taken from the weight list to assure that nothing is left out or counted twice. Also, changes made to update the master list are easily transferred to the computer input list. A list of items corresponding to the drawing tree clearly satisfies the bookkeeping requirement. It also satisfies a convenience of calculation requirement because the drawing tree is organized largely on the basis of assembly sequence. Thus it consists of physically removable assemblies which are, in turn, made up of smaller physically removable assemblies. Usually at some level of detail, a convenient package for the calculation of local mass properties is listed.

At specified intervals, all the estimates were brought up to date and submitted to the computer for calculation of composite spacecraft mass properties. A report was made that consisted of a weight summary, a table of spacecraft mass properties for several configurations, a copy of the weight list by drawing tree, and a copy of the weight list by subsystem. The weight summary was a tabulation of the total separated weight (adapter is not included) of each subsystem and a total spacecraft weight. Changes from the previously reported weight were explained. The table of mass properties lists weight, center of mass, and moments and products of inertia for the spacecraft in each of several standard configurations.

4. Measurement Activities

In the *Mariner* Mars 1969 calculations, weight and center-of-mass were both calculated and measured; the inertias were calculated only. The propulsion subsystem on *Mariner* Mars 1971 is much larger and relocated from the *Mariner* Mars 1969 position. The result was that the x-y axis center-of-mass test fixtures were still suitable, but the z axis center-of-mass fixture was not. Additionally, the *Mariner* Mars 1971 gimballed motor provides more thrust axis control than the *Mariner* Mars 1969 jet vanes. These factors greatly reduced the accuracy requirements on the z center of mass.

Based on these calculations the plan for *Mariner* Mars 1971 mass properties determination was formed. The desired accuracies for final determination of mass properties were established. These are based only on *Mariner* Mars 1969 experience and existing measurement and calculation capabilities. The weight and x-y center-of-mass of the assembled spacecraft are measured on the proof-test model (PTM) and on the flight spacecraft.

The PTM measurements are made both wet and dry (with and without referee fluids simulating the propellants), but those for the flight spacecraft are measured dry only. The dry measurements are to provide the final values for weight, x and y, since the measured values are better than the calculations. The center-of-mass along the z axis will not be experimentally determined. In addition, the actual measurements will show differences between spacecraft, which the calculations do not.

Another reason for the measurements is to build confidence in the calculations. For example, if the measured values of x and y agree within 0.10 in. of the calculated values, and if the measured value is known to 0.05 in., then the calculations of x and y will be accurate to 0.15 in. Since the method of calculating z is the same for calculating x and y, it is reasonable that z is also accurate to 0.15 in. Agreement between calculated values for weight and locations (x and y) also implies correctness of inertias. Measurement of the referee propellant-loaded PTM provided another verification: agreement between the calculated weight and center-of-mass of the wet PTM (starting from the measured dry weight and center-of-mass) with the measured values would demonstrate that the liquids can be analytically added to the dry spacecraft, making the measurement of a fueled spacecraft unnecessary.

The test set-up for measuring spacecraft weight and x-y center of mass is shown in Fig. 1. The assembled

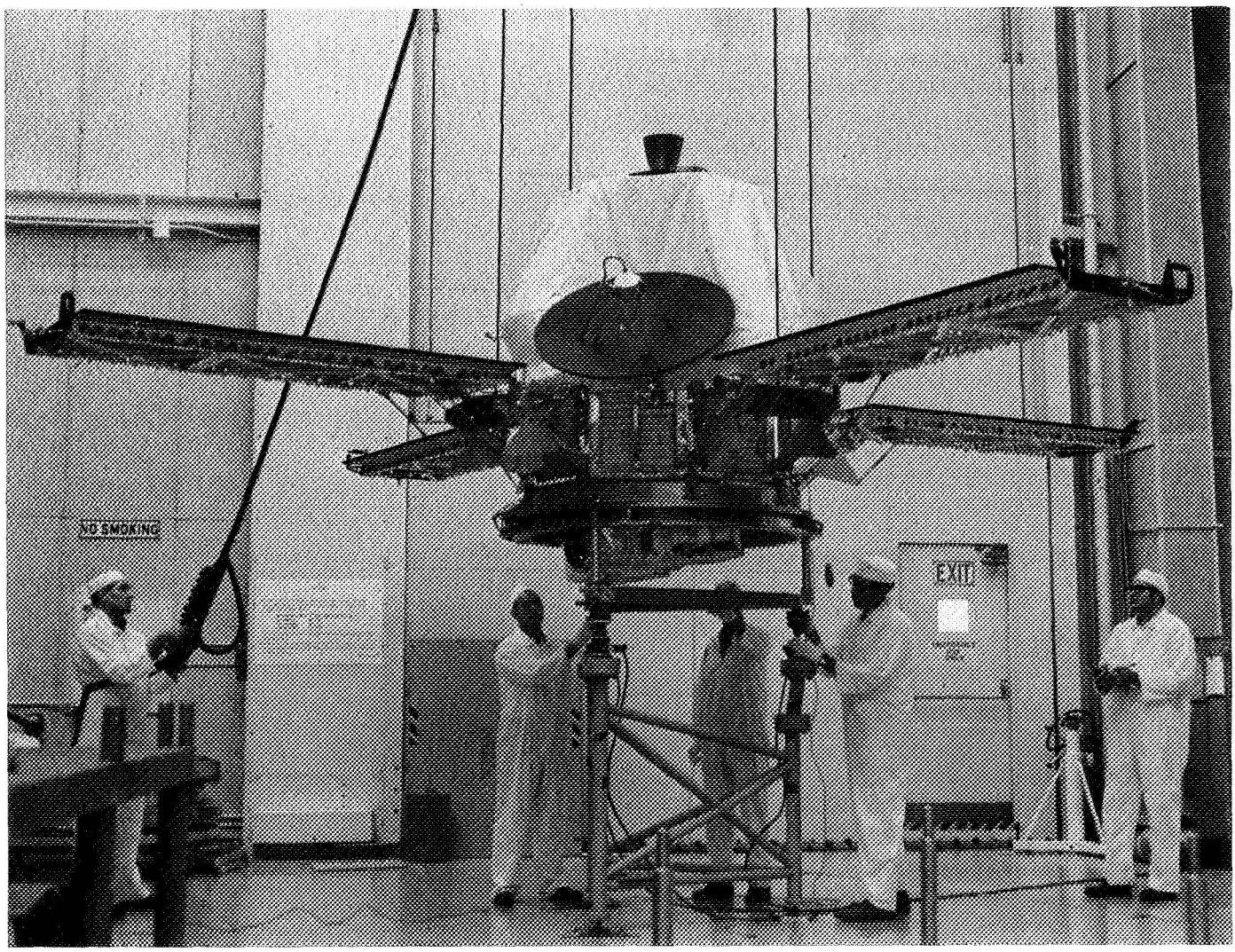

Fig. 1. Mariner Mars 1971 weight and center-of-mass test

spacecraft mounted on its support ring is attached to a fixture which adapts to the three-point center-of-mass test stand. Three Baldwin-Lima-Hamilton C3P1 load cells (1000-lb capacity) are used as forced transducers. The load cells are mounted on horizontal bearing plates, so that they are free to move horizontally. They are positioned accurately by the center-of-mass adapter through a cup-and-ball arrangement. The measurements are made in each of the three possible 120-deg-spaced positions. This eliminates errors in center-of-mass should the center-of-mass stand be slightly out-of-level, or should any load cell be slightly in error. The support ring center-of-mass is eliminated from the equations (used to reduce the data) by repeating the sequence of three weighings with the spacecraft rotated 180 deg relative to the adapter. The weighing operations require approximately 4 h.

A simple error analysis indicated that the accuracy of the measurements is approximately ± 3 lb in weight and ± 0.040 in. in x and y. Because the measurements are made in air, a correction for buoyancy is required: 1.91 lb, of which 1.41 lb is due to propulsion subsystem tankage.

5. Results

A comparison between measured and calculated values is given in Table 1. The dry spacecraft values assume no propellants, pressurants, or attitude-control gas.

Table 1. Measured and calculated values

	Weight, lb	x, in.	y, in.
Dry Spacecraft			
Calculated	1115.3	−0.110	0.220
Measured	1114.4	−0.182	0.068
Difference	0.9	0.072	0.152
Wet Spacecraft			
Calculated	2175.0	1.697	−1.755
Measured	2172.2	1.701	−1.755
Difference	2.8	−0.004	0.000

The desired accuracy requirements for weight W, x and y are:

$$\left|\frac{\Delta W}{W}\right| < 0.0025$$

$$(\Delta x)^2 + (\Delta y)^2 < 0.01 \text{ in.}^2$$

where ΔW, Δx and Δy are the uncertainties in W, x and y. Since the measured values of x and y are within 0.040 in. of the correct values, the above calculated x and y fall slightly outside the specification. While this was a disappointment, no refinement of the calculations was made for two reasons: the better measured values were available, and the calculations were adequate for the remaining properties, whose accuracy requirements were less.

I. Structure and Dynamics Test and Analysis,
Applied Mechanics Section

1. Electronic Analog Simulation

Dynamic test implementation problems encountered during forced vibration testing of the *Mariner* Mars 1971 propulsion module necessitated an evaluation of the capability of the peak select acceleration control system. One phase of this evaluation was done with the aid of an analog computer which simulated the dynamic characteristics of the propulsion module and vibration exciter and the vibration exciter and amplifier electrical characteristics. The dynamic characteristics of the primary propulsion system (PSS) structure were represented by twelve normal modes obtained from digital computer analysis. The dynamics of the vibration exciter, i.e., the armature flexures and trunnions, were obtained experimentally by accomplishing a modal survey of the system supporting a dummy structure of known inertial properties. Electrical characteristics of the vibration exciter and amplifier system were obtained from the manufacturer. The peak select acceleration control unit was connected directly to the analog simulation, as shown in Fig. 1, using the actual sweep oscillator and servo-control system. This configuration of analog simulation of the structure and vibration exciter test and control equipment provided the capability of varying test parameters, such as structural damping, structural shaker frequencies, sweep rate, compressor speeds and others, and evaluating the effects of these parameter changes on the peak select control unit in real-time.

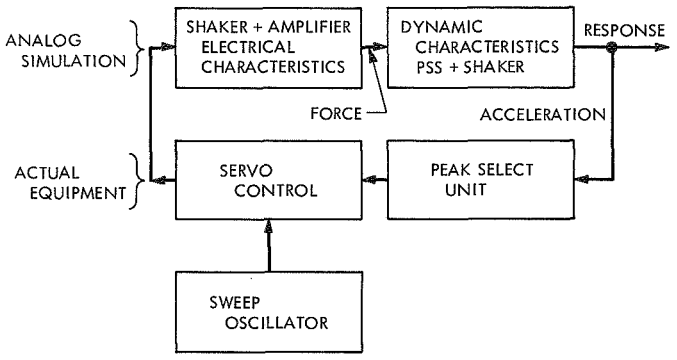

Fig. 1. Block diagram of analog and test equipment

Eight control accelerometers located at the structure-fixture interface and two response control accelerometers located on the two propellant tank hubs as simulated by the analog were used for test control evaluation. Figure 2 is a typical representation of switching between control transducers to maintain a preset amplitude at one or more control points.

Although the exact test conditions of the real test were not completely simulated, the similarity of control switching and slope, i.e., rate of change of correction, were sufficient to evaluate and demonstrate that the control system as used was marginally adequate to satisfy the objectives of the intended test program.

The uniqueness of the evaluation performed was the combination of the real-time analog simulation of the test structure and shaker system with the actual test control system. Many kinds of parametric changes were

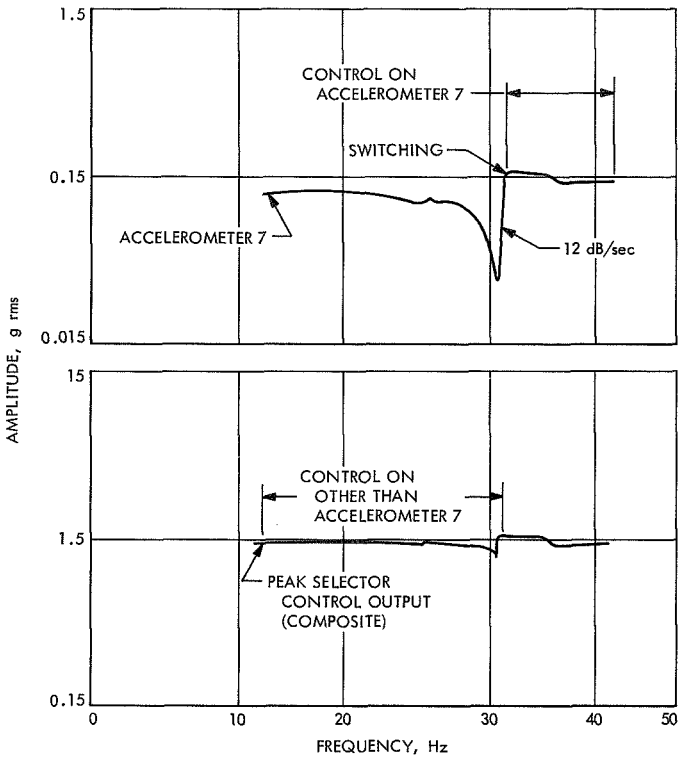

Fig. 2. Comparison of control accelerometer 7 and peak selector output

made using real-time test sweeps without endangering the test structure or shaker system.

The ability to make parametric changes to a complicated control system in a timely manner has been demonstrated and should prove to be of value in future flight programs.

J. Codispersion Propellant Expulsion Bladder Evaluation, *Materials Section*

1. Introduction

During early developmental testing of the *Mariner* Mars 1971 propulsion subsystem expulsion bladders a series of failures occurred resulting in substantial changes in both materials, fabrication techniques, and configuration at launch. The bladder is a flexible TFE-FEP Teflon laminate membrane which fits inside a 30-in.-diam titanium propellant tank and is pressurized by nitrogen gas to expel propellants contained within under zero g conditions. It is constructed by spraying Teflon dispersions onto an aluminum mandrel which is leached out chemically after fusion of the laminate layers. The standard laminate bladder was found to be significantly degraded by solvent stress-cracking in Freon TF (used as propellant referee fluid), particularly in a biaxial cyclic stress field. Similar behavior could be predicted for the actual propellant, based upon surface wetting and swelling similarities. Subsequent replacement of the solvent-sensitive FEP Teflon Type T-120 in

the laminate with a superior type TE-9511 (higher molecular weight) was a major advancement in reducing solvent sensitivity. Changes in construction of the laminate to a codispersion system were also critical to the success of the bladder redesign (See Fig. 2 in *Subsection G).*

This report summarizes some of the significant test results on the codispersion material derived prior to production of flight bladders of this type.

2. Test Program

Tensile testing of samples from an actual bladder revealed a significant improvement in uniaxial ultimate strength values (Table 1). Testing of samples immersed in actual propellants was accomplished by soaking test samples without load for 165 h in monomethylhydrazine (MMH) or inhibited nitrogen tetroxide (N_2O_4). The samples were removed, wiped dry, and tested within 2 min. Results are shown in Table 2. The N_2O_4 propellant was observed to have a plasticizing effect on Teflon (lower apparent modulus). This is unlikely to affect performance in this application.

Measurement of fluid linear swelling effects on the codispersion material was conducted by optical determination of length change of laminate strips in glass holding fixtures immersed in propellant and referee fluids for various times up to 303 h. This information is important to sizing bladders for fitting tank interior dimensions. The results are presented in Table 3. Both isopropyl alcohol and MMH are shown to have no swelling effect, while N_2O_4 and Freon TF show swelling characteristics at different rates. N_2O_4 swelling stabilizes within 24 h, while Freon TF requires more than 5 days.

Fatigue tests between zero and various tension stresses were performed on codispersion laminate material, revealing that stresses in excess of 3000 psi were necessary to produce failure in air within 1000 cycles. Launching with pressure within the bladders will reduce cyclic stresses to very low levels easily withstood by the codispersion laminate material.

Numerous samples have been studied using thin sections viewed with transmitted polarized light for revealing interlayer characteristics in an effort to understand the behavior of this material in the bladder application. A typical microstructure is shown in Fig. 1. The "balanced" structure obtained is believed to produce lower surface residual stresses in the finished product than standard bladder laminates. Residual stresses result from contraction differences between FEP and TFE Teflon during cooling from the fusion cycles while restrained by the aluminum mandrel. Standard laminates have maximum residual stress on the "outer" FEP surface, while codispersion laminate material appears to confine residual stress from this effect to "interior" interfaces.

Table 1. Bladder material uniaxial ultimate strength values

Type	Yield strength, psi	Ultimate strength, psi	Elongation, %
Codispersion laminate (typical values)	1860	4430	450
Standard laminate (typical values)	1800	3600	425

Table 2. Bladder motor uniaxial ultimate strength values after exposure to propellants

Type	Yield strength, psi	Ultimate strength, psi	Elongation, %
Codispersion laminate in MMH	1830	4800	488
Codispersion laminate in N_2O_4	733	4000	541

Table 3. Fluid linear swelling effects on codispersion bladder material

Liquid	Percent of length change after time lapses				
	14.5 h	42.5 h	62.5 h	138.5 h	303 h
Inhibited N_2O_4	1.57	1.60	1.60	1.60	1.60
Inhibited N_2O_4	1.60	1.60	1.60	1.60	1.60
MMH	0	0	0	0	0
MMH	0	0	0	0	0
Isopropyl alcohol	0	0	0	0	0
Isopropyl alcohol	0	0	0	0	0
Freon 113 (TF)	0.20	0.63	1.22	2.44	2.44
Freon 113 (TF)	0.24	0.83	1.34	2.49	2.49

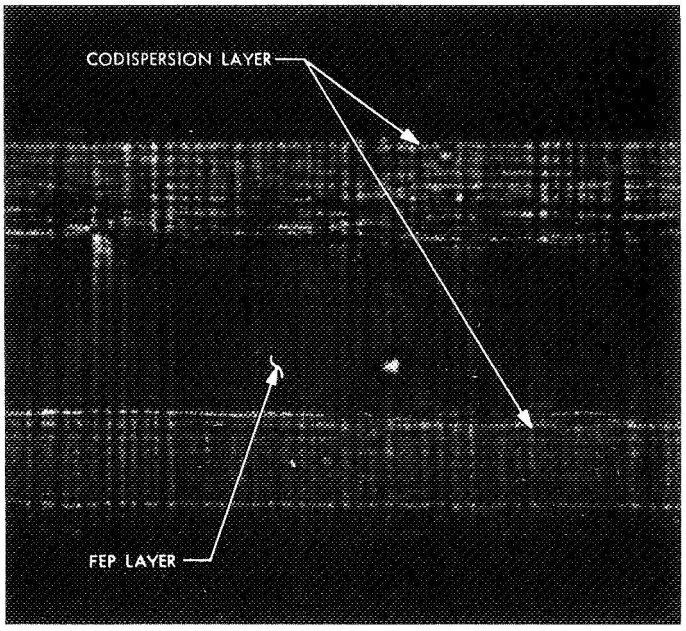

POLARIZED ILLUMINATION
MAGNIFIED 200 X

Fig. 1. Microstructure of new codispersion expulsion bladder material

K. Evaluation of Spacer Rod Material for Narrow-Angle Television Camera, *Materials Section*

1. Introduction

The *Mariner* Mars 1971 narrow-angle television camera employs a spring-loaded spacer system to maintain dimensional requirements between critical optical elements. The spacers are 0.3-in.-diam by 10 in. long, spring-loaded in compression to 6000 psi. The working temperature range is −25 to +35°C (−11 to +95°F). The maximum permissible change in length of the spacer rods is 0.002 in. to maintain the focusing requirements.

To meet the above requirements, a material with a maximum creep rate of 20 μin./in./y when stressed at 6000 psi in compression and a coefficient of expansion of less than 4.0×10^{-7}/°C (2.2×10^{-7}/°F) in the range of −25 to +35°C (−11 to +95°F) is required. Super Invar was selected because published physical properties data indicated it to have the best promise of meeting the requirements (Refs. 1, 2).

Of concern was the dimensional change associated with a reported (Ref. 2) phase change from face-centered cubic to body-centered cubic at −10°C (+14°F). An increase of nickel content lowers the temperature for the start of this phase change. A Super Invar composition yielding a phase change temperature well below the −25°C (−11°F) working temperature, was considered a requirement to provide a safe margin to avoid such a dimensional change.

2. Material Composition and Verification

Super Invar rod, 0.3-in.-diam, Heat No. J-6055, was procured from Simonds Steel Div. of Wallace-Murray Corp. The material as-received had been annealed at 760°C (1400°F), followed by air cooling. The chemical composition of a heat melt sample, as reported by the manufacturer, is as follows:

C	*P*	*S*	*Si*	*Mn*	*Ni*	*Cr*	*Cu*	*Co*	*Fe*
0.08	0.010	0.005	0.13	0.50	32.38	0.05	0.06	5.11	Balance

Chemical analysis was verified on three separate lengths of rod selected at random.

Metallographic sections were made to determine the grain structure. A typical microstructure is shown in Fig. 1.

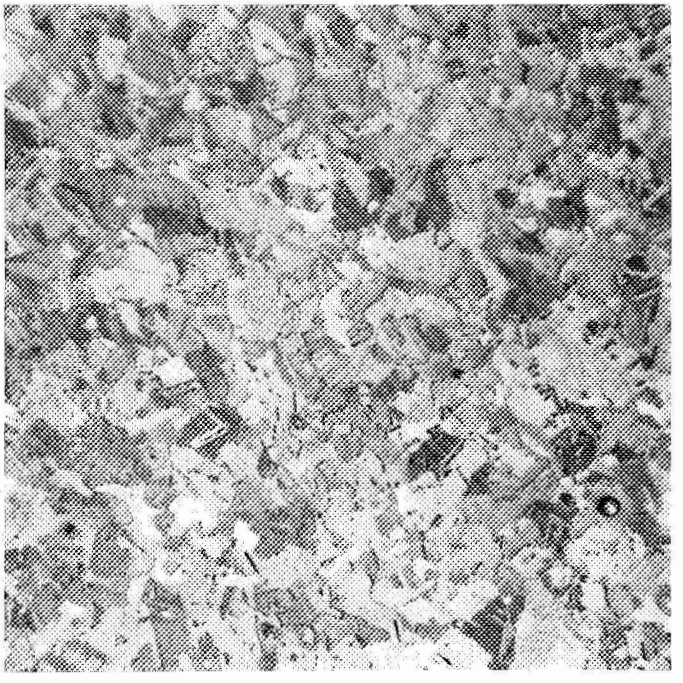

MAGNIFIED 500 X

Fig. 1. Microstructure of Super Invar

3. Test Program

The following tests were made on random samples to verify materials requirements and obtain property data:

Thermal coefficient of expansion (Fig. 2)

Plastic microstrain in compression (Fig. 3)

Compressive microcreep at 6000 psi (Fig. 4)

Tensile yield (0.2% offset) and tensile strength (Table 1)

Knoop microhardness (Table 2)

All specimens were machined and heat-treated according to the following schedule:

(1) 829 to 843°C (1525 to 1550°F) for 1/2 h with H_2O quench.

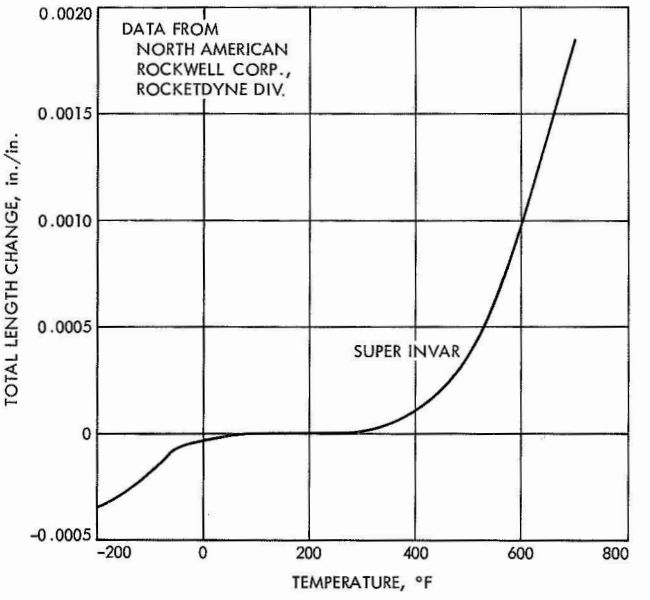

Fig. 2. Thermal expansion properties of Super Invar

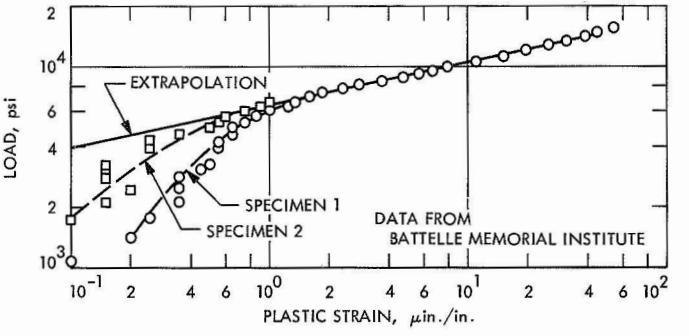

Fig. 3. Compression microstrain data

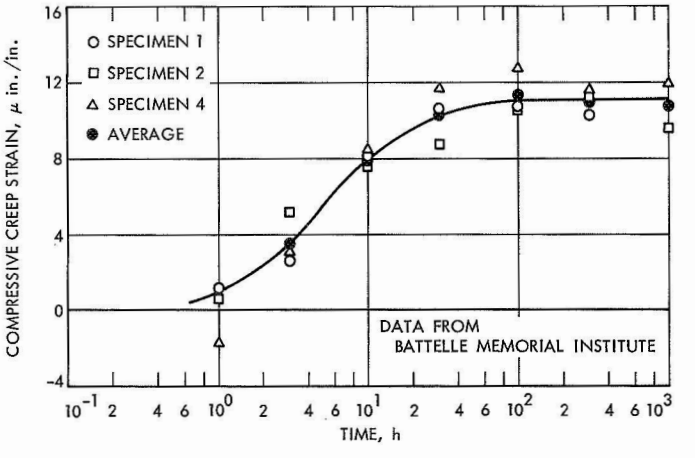

Fig. 4. Compressive microcreep data

(2) Specimens were machined.

(3) 316 ± 5°C (600 ± 10°F) for 1 h and air cooled.

(4) 96 ± 3°C (205 ± 5°F) for 48 h and air cooled.

(5) 189 ± 5°C (375 ± 10°F) for 16 h and air cooled (to simulate application of dry film lubricant to spacer rods).

4. Discussion

A plot of change of length versus temperature (Fig. 2) shows linear expansion in the ranges −45 to +21°C (−50 to +70°F) and +21 to +125°C (+70 to +275°F) with coefficients of expansion of 8.8×10^{-7}/°C (4.9×10^{-7}/°F) and zero, respectively. The change of length over the working temperature range of −25 to +35°C (−11 to +95°F) is 0.000040 in./in., which corresponds to a coefficient of expansion of 6.7×10^{-7}/°C (3.7×10^{-7}/°F). The phase change shown in Fig. 2 at −45°C (−50°F) is well below the working temperature of −25°C (−11°F) and, therefore, is not relevant to the application as a television camera spacer rod.

The microyield strength (stress to produce 10^{-6} plastic strain) was found to be 6000 and 6600 psi for two specimens tested (Fig. 3). The logarithmic plot of stress versus plastic strain is linear for strains above 10^{-6}, but concave downward for lesser strains. Microcreep under compressive stresses of 6000 psi for up to 1000 h showed initial rates of approximately 0.8×10^{-6}/h (Fig. 4). After approximately 30 h and a total strain of approximately 11×10^{-6}, microcreep ceased. The nonlinearity of the logarithmic stress–plastic strain data and the transient behavior of the creep data are believed to be related to the residual stresses contained in the machined surface layers of the specimens.

Tensile yield and ultimate strength data (Table 1) indicate good uniformity of strength properties in the randomly selected specimens. The largest variations in average tensile yield and tensile ultimate values were 5.5 and 4.5%, respectively. The values correlate with data given in Ref. 1.

The Knoop microhardness tests made on randomly selected specimens (Table 2), show good material uniformity throughout the specimen cross sections. The microstructural examinations of the rods showed the uniform fine-grained structure desirable for this material.

All the data indicate that the Super Invar material is satisfactory for the intended application as spacer rods. Microcreep is well within design requirements for the

Table 1. Tensile properties of Super Invar rods

Sample No.	Tensile yield strength (0.2% offset)		Tensile ultimate strength		Elongation at failure		Number of specimens
	Average, ksi	Range, ksi	Average, ksi	Range, ksi	Average percent	Range percent	
1B	55.0	54.6–55.3	80.6	80.1–81.0	40	39–41	3
2B	54.2	53.6–54.6	79.0	78.8–79.1	41	39–42	3
3B	55.4	55.0–56.0	80.1	79.1–80.8	44	41–48	3
4B	54.0	53.9–54.1	80.0	79.6–80.3	44	44–45	3
5B	54.5	53.7–55.2	79.8	79.1–80.3	41	39–42	3
6B	54.3	53.7–55.2	79.4	78.4–80.1	41	41–42	3
7B	53.3	52.9–53.6	79.6	78.6–80.1	41	41–42	3
8B	53.0	52.9–53.2	78.3	78.1–78.4	43	42–44	3
9B	54.3	53.8–55.0	80.2	79.8–80.6	43	41–44	3
10B	52.5	51.8–53.6	77.1	76.1–78.6	40	39–42	3
Average	54.0	51.8–56.0	79.4	76.1–81.0	42	39–48	

Table 2. Knoop microhardness of Super Invar rods[a]

Specimen No.	Distance from edge, in.	Knoop hardness No.
1B	0.001	155.2 (average of two specimens)
	0.002	192.4
	0.003	204.0
	0.004	190.2
	0.005	209.0
	0.006	211.6
	0.007	209.0
	0.008	199.2
	0.009	199.2
	0.150	186.7 (average of five specimens)
8A	0.150	187.7 (average of five specimens)

[a]100-g load, 40 X objective lens.

specific *Mariner* Mars 1971 TV use. Coefficient of expansion is very low (although slightly higher than the optimum requirement) over the entire working temperature range and is actually zero in the range of +21 to +135°C (+70 to +275°F). The phase change at approximately −45°C (−50°F) provides a safe margin well below the working temperature range of the camera.

References

1. *Mechanical and Physical Properties of Invar and Invar-Type Alloys*, Defense Metals Information Center Memorandum 207, Battelle Memorial Institute, August 31, 1965.
2. Scott, H., "Expansion Properties of Low-Expansion Fe-Ni-Co Alloys," *Trans. AIME*, Inst. Metal Div., Vol. 89, pp. 506–537, 1930.